The chromatin-associated 53BP1 ortholog, HSR-9, regulates recombinational repair and *X* chromosome segregation in the *Caenorhabditis elegans* germ line

Qianyan Li*[1,2], Sara Hariri*[1,2], Aashna Calidas[1], Arshdeep Kaur[1], Erica Huey[1], and JoAnne Engebrecht[1,2,3]

*Contributed equally

[1]Department of Molecular and Cellular Biology

[2]Biochemistry, Molecular, Cellular and Developmental Biology Graduate Group

University of California Davis

Davis, California 95616

[3]Corresponding author: Department of Molecular and Cellular Biology, and Biochemistry, Molecular, Cellular and Developmental Biology Graduate Group, University of California Davis, One Shields Ave., Davis, CA 95616. E-mail: jengebrecht@ucdavis.edu

Running title: Role of HSR-9 in meiosis

ABSTRACT

53BP1 plays a crucial role in regulating DNA damage repair pathway choice and checkpoint signaling in somatic cells; however, its role in meiosis has remained enigmatic. In this study, we demonstrate that the *Caenorhabditis elegans* ortholog of 53BP1, HSR-9, associates with chromatin in both proliferating and meiotic germ cells. Notably, HSR-9 is enriched on the *X* chromosome pair in pachytene oogenic germ cells. HSR-9 is also present at kinetochores during both mitotic and meiotic divisions but does not appear to be essential for monitoring microtubule-kinetochore attachments or tension. Using cytological markers of different steps in recombinational repair, we found that HSR-9 influences the processing of a subset of meiotic double strand breaks into COSA-1-marked crossovers. Additionally, HSR-9 plays a role in meiotic *X* chromosome segregation under conditions where *X* chromosomes fail to pair, synapse, and recombine. Together, these results highlight that chromatin-associated HSR-9 has both conserved and unique functions in the regulation of meiotic chromosome behavior.

Article Summary

While 53BP1 is known for its crucial role in DNA damage signaling and repair in somatic cells, its role in meiosis is not well understood. Li, Hariri, et al., show that *C. elegans* 53BP1 not only functions in meiotic recombination and checkpoint signaling but also regulates the transmission of sex chromosomes when meiosis is perturbed. These results highlight the importance of 53BP1 in *C. elegans* meiosis and suggest that 53BP1 has both conserved and organism-specific functions.

Introduction

The tumor suppressor 53BP1 regulates several biological processes important for genome integrity, including transcription, DNA repair, and chromosome segregation (Mirza-Aghazadeh-Attari et al., 2019). It was originally identified as a p53 interacting protein (53 Binding Protein 1) (Iwabuchi et al., 1994) and was subsequently shown to promote p53-DNA interactions to enhance transcription and checkpoint signaling (Cuella-Martin et al., 2016). Many studies have focused on the role of 53BP1 in DNA repair. 53BP1 binds and protects DNA ends from resection in complex with RIF1, the Shieldin complex, and PTIP, thereby promoting non-homologous end joining (NHEJ), and antagonizes RAD51 filament formation post-resection to inhibit homologous recombination (HR) (Callen et al., 2020; Chapman et al., 2013; Escribano-Diaz & Durocher, 2013; Mirman et al., 2018; Noordermeer et al., 2018; Ward, Minn, van Deursen, et al., 2003). Its role in promoting NHEJ was reinforced by the finding that mutation of 53BP1 can partially suppress the embryonic lethality of *Brca1* mutant mice, which is proposed to be due to the inappropriate use of NHEJ when homologous recombination (HR) is inhibited by *Brca1* mutation (Bouwman et al., 2010; Bunting et al., 2010; Cao et al., 2009; Chen et al., 2020; Li et al., 2016). 53BP1 has also been shown to play important roles in class switch recombination and telomere protection (Difilippantonio et al., 2008; Dimitrova et al., 2008; Rocha et al., 2016; Sundaravinayagam et al., 2019; Ward et al., 2004). In addition, 53BP1 monitors microtubule-kinetochore interactions or tension, which are important for proper chromosome segregation (Jullien et al., 2002; Wang et al., 2017; Yim et al., 2017).

53BP1 is chromatin-associated and becomes enriched at double-stranded breaks (DSBs) together with the histone variant, γ–H2AX (Ward, Minn, Jorda, et al., 2003). In fact, 53BP1 is often used as a marker of DSB formation. At DSBs, 53BP1 has been shown to bind to histone H4 lysine 20 dimethylation (H4K20me2) through its conserved Tudor domain and H2A lysine 15 ubiquitination (H2AK15ub) (Botuyan et al., 2006; Fradet-Turcotte et al., 2013). In yeast, the 53BP1 ortholog, Rad9, associates with histone H3 lysine 79 methylation (H3K79me) at DSBs and regulates strand annealing for crossover recombination (Ferrari et al., 2020). Recent work provides evidence that 53BP1 undergoes liquid-liquid phase separation both in the context of DNA repair and transcriptional regulation (Kilic et al., 2019; Zhang et al., 2022), suggesting that 53BP1 has complex and incompletely understood chromatin interactions.

Recombinational repair in the context of unique chromatin structure is critical for successful meiosis. Despite the known association of 53BP1 with specific chromatin marks (Botuyan et al., 2006; Fradet-Turcotte et al., 2013) and its role in DNA repair (Callen et al., 2020; Chapman et al., 2013; Escribano-Diaz & Durocher, 2013; Mirman et al., 2018; Noordermeer et al., 2018; Ward, Minn, van Deursen, et al., 2003), very few studies have explored the role of 53BP1 in meiosis. Meiotic recombination is initiated by the intentional induction of DSBs by the conserved topoisomerase Spo11 (Dernburg et al., 1998; Keeney et al., 1997). The broken ends are then processed by multiple exonucleases to expose a 3’ single-stranded tail for strand invasion mediated by the recombinases Dmc1 and Rad51 (in many organisms), or RAD-51 alone (in *C. elegans*). Following strand invasion, while both non-crossover and crossover repair outcomes are possible, at least one DSB per chromosome pair must be converted into an

interhomolog crossover for proper chromosome segregation (Chen & Weir, 2024; Gartner & Engebrecht, 2022).

53BP1 mutant mice exhibit growth retardation and increased cancer susceptibility yet are fertile, suggesting that 53BP1 does not play an essential role in meiosis (Ward, Minn, van Deursen, et al., 2003). Further, DNA end resection is not affected in mouse spermatocytes lacking 53BP1 (Paiano et al., 2020). In yeast meiosis, Rad9 binds to exogenously induced DSBs but not to Spo11-induced breaks (Usui & Shinohara, 2021). In *C. elegans*, mutation of *hsr-9* (*53BP1*) enhances the phenotype of *brc-1*(*BRCA1*) mutations, instead of suppressing lethality as in mammals, suggesting it may not promote NHEJ (Hariri et al., 2023). HSR-9 has been shown to play a role in repair and signaling of exogenous breaks in the germ line (Ryu et al., 2013); however, its role in meiotic DSB repair or checkpoint signaling has not been reported. Thus, the function of 53BP1 in meiosis remains unclear and may vary across organisms.

Here, we take advantage of the *C. elegans* system to examine the role of HSR-9 in the germ line. We find that HSR-9 is chromatin-associated, enriched on the *X* chromosome pair in oogenic germ cells, and present at kinetochores in cells undergoing mitotic and meiotic divisions. Mutant analyses reveal roles for HSR-9 in the processing of meiotic DSBs into crossovers and in germline apoptosis. Additionally, HSR-9 is important for segregation of the *X* chromosome pair in oogenic germ cells when pairing, synapsis, and recombination are defective.

Materials and Methods

Genetics

C. elegans strains used in this study are listed in Table S1. Some nematode strains were provided by the Caenorhabditis Genetics Center, which is funded by the National Institutes of Health National Center for Research Resources (NIH NCRR). Strains were maintained at 20°C except for *zyg-1(ts)*, which was maintained at 15°C.

CRISPR-mediated allele construction

hsr-9(xoe17) in *rad-54* and the Hawaiian background used for SNP mapping was generated as previously reported (Hariri et al., 2023). *gfp::v5::hsr-9 (xoe45)* was generated using the CRISPR-Cas9 ribonucleoprotein complexes based on the co-CRISPR method (Paix et al., 2015). A 1324bp double strand DNA fragment was synthesized (Gblock; IDT) and used as the repair template after PCR amplification. This repair template contains sequences for GFP, V5 tag, and flexible linkers, flanked by 5' and 3' homology arms of 175 and 198 bps, respectively. Insertion of GFP, V5 and the flexible linkers upstream of the start codon disrupted the PAM sequence, eliminating the need for point mutations to disrupt the guide RNA sequence. Briefly, the Cas9-crRNA-tracrRNA ribonucleoprotein complex, along with the repair template, was microinjected into the *C. elegans* gonad. F1 progenies exhibiting roller/dumpy phenotypes were isolated and genotyped by PCR to confirm GFP insertion. Similarly, *gfp::hsr-9::3xHA (xoe47)* was generated using a 1290bp double-strand DNA repair template to insert the flexible linker-GFP-3xHA sequence before the stop codon. A silent mutation was

138 introduced at the junction of the 5' homology arm and the flexible linker sequence to
139 disrupt the PAM sequence in the repair template. Guide sequences, repair templates,
140 and genotyping primers for both fusions are provided in Table S2. All strains were
141 outcrossed for a minimum of three times before analyses.
142
143 ***Embryonic lethality and male self-progeny***
144 L4 stage hermaphrodites were placed on individual plates and allowed to lay eggs. After
145 24hrs, they were transferred to new plates and this process was repeated for 3 days.
146 Embryonic lethality was determined by counting eggs and hatched larvae 24hrs after
147 removing the adult hermaphrodite and percent was calculated as eggs/(eggs + larvae).
148 Males were scored 72hrs post adult removal and percent was calculated as males/(males
149 + hermaphrodites + eggs).
150
151 ***Cytological analyses***
152 For live cell imaging, hermaphrodites aged 18–24hrs post L4 stage were anesthetized in
153 1mM tetramisole (Sigma-Aldrich) and immobilized between a coverslip and a 2% agarose
154 pad on a glass slide. Z-stacks (0.33µm) were captured on a spinning-disk module of the
155 Marianas spinning-disk confocal real-time 3D Confocal-TIRF microscope (Intelligent
156 Imaging Innovations) equipped with an 63x, NA 1.46 objective lens using a Photometrics
157 QuantiEM electron multiplying charge-coupled device (EMCCD) camera, a Zeiss 980
158 LSM with Airyscan 2 equipped with a 63x 1.4NA objective and the Airyscan Multiplex
159 Super-Resolution-4Y mode, or an API Delta Vision Ultra deconvolution microscope
160 equipped with an 60x, NA 1.49 objective lens. Subsequent Airyscan processing was

161 performed with automatic settings. Z-projections of stacks were generated, cropped, and
162 adjusted for brightness in Fiji.

163 Immunostaining of germ lines was performed as described (Jaramillo-Lambert et al.,
164 2007) except slides were incubated in 100% ethanol instead of 100% methanol for
165 detection of direct fluorescence of GFP::COSA-1, mCherry::HIM-8, and GFP::RPA-1.
166 For fixed images of GFP::V5::HSR-9, dissected gonads were rapidly immersed in liquid
167 nitrogen and then fixed with 2% paraformaldehyde as in (Janisiw et al., 2020). Primary
168 antibodies are listed in Table S3. Life Technologies secondary donkey anti-rabbit
169 antibodies conjugated to Alexa Fluor 488 or 594 and goat anti-rabbit conjugated to
170 Alexa Fluor 647 were used at 1:500 dilutions. DAPI (2μg/ml; Sigma-Aldrich) was used to
171 counterstain DNA.

172 Collection of fixed images was performed using an API Delta Vision Ultra
173 deconvolution microscope. Z stacks (0.2 μm) were collected from the entire gonad. A
174 minimum of three germ lines was examined for each condition. Images were
175 deconvolved using Applied Precision SoftWoRx batch deconvolution software and
176 subsequently processed and analyzed using Fiji (ImageJ) (Wayne Rasband, NIH).
177 Images show half-projections of gonads.

178 To determine the *X*/autosome ratio of GFP::V5::HSR-9 fluorescence, the GFP
179 fluorescence intensity was measured by drawing a region of interest (ROI) around the *X*
180 chromosomes in pachytene nuclei. The intensity was also measured using the same
181 ROI in an area within the same nucleus that excluded the *X* chromosomes. For H3S10P
182 quantification, nuclei positive for H3S10P signal were counted in the proliferative zone
183 of germ lines from age-matched 18hr post-L4 hermaphrodites grown at 25C to

inactivate *zyg-1*. GFP::RPA-1 fluorescence was quantified by measuring the mean fluorescence intensity and standard deviation (SD) in Fiji for individual nuclei from transition zone to mid-pachytene. Coefficient of variation (CV) was calculated as SD of intensity divided by mean intensity (Bishop et al., 2015). For RAD-51 quantification, germ lines were divided into the transition zone (leptotene/zygotene, from the first to last row with two or more crescent-shaped nuclei), and pachytene (divided into 3 equal parts: early, mid, and late pachytene). RAD-51 foci per nucleus was scored from half projections of the germ lines for each divided region. CHK-1Ser345p foci were quantified in early pachytene nuclei. GFP::COSA-1 foci were scored from deconvolved 3D z-stacks in mid-late pachytene nuclei individually to ensure that all foci within each individual nucleus were counted. mCherry::HIM-8 foci were quantified from deconvolved 3D z-stacks throughout the germline.

Meiotic mapping

Meiotic crossover frequencies and distribution were assayed utilizing single-nucleotide polymorphism (SNP) markers as in (Nabeshima et al., 2004). The SNP markers located at the boundaries of the chromosome domains were chosen based on data from WormBase (WS231), (Bazan & Hillers, 2011), and (Saito et al., 2013) and are indicated in Figure 5D. The SNP markers and primers used are listed in (Li et al., 2020). PCR and restriction digests of single worm lysates were performed as described in (Li et al., 2020).

X chromosome nondisjunction

Hybrid hermaphrodites expressing GFP::2xNLS and tdTomato::H2B (fusions inserted into the same location on each of the *X* chromosomes) were mated to *fem-3(e1996)/*nT1GFP; *lon-2(e678)* males. Parents were transferred every 24hrs for 3 days. Progeny were scored for GFP and tdTomato on a fluorescent stereo microscope at 20x magnification on day 3. Only worms with green-fluorescent pharynxes were scored for *X* chromosome markers to ensure cross progeny were examined.

Statistical analyses

Statistical analyses and figures were prepared using GraphPad Prism version 10.0 (GraphPad Software). Statistical comparisons of embryonic lethality (Figure S1B, Figure S2A, and Figure 6A), *X*/autosomal GFP::V5::HSR-9 fluorescence intensity (Figure 2E), H3S10P nuclei/germ line (Figure 3D), GFP::RPA-1 fluorescence (Figure 4C and Figure S2B), RAD-51 foci numbers (Figure 4E, G and Figure S2C), % male self-progeny, pCHK-1 foci/nucleus and apoptotic nuclei/gonad (Figure 6B-E) were analyzed by Mann-Whitney. Chi-squared test was used for statistical analyses on GFP::COSA-1, genetic map distance, distribution, and % oocytes with X chromosome non-disjunction events (Figure 5A, D, and Figure 7B). Detailed descriptions of statistical analyses are indicated in figure legends.

Results

HSR-9 associates with chromatin in the germ line

HSR-9 exhibits a domain structure similar to human 53BP1, with an intrinsically disordered N-terminus and conserved BRCT domains at the C-terminus. The predicted structure of HSR-9 as determined by AlphaFold is shown in Figure 1A (Jumper et al., 2021) and the extent of disorder is shown in Figure 1B (Erdos et al., 2021). To examine HSR-9 localization, we constructed GFP fusions to both the N and C-termini of HSR-9 using CRISPR genome editing (Figure S1A). Mutation of HSR-9 has no effect on progeny viability (Ryu et al., 2013), and we confirmed this using the putative null allele *hsr-9(xoe17)* (Hariri et al., 2023) (Figure S1A). We examined the functionality of the GFP fusions to HSR-9 by monitoring embryonic lethality in the absence of the ortholog of the tumor suppressor BRCA1/BRC-1, as the *hsr-9; brc-1* double mutant results in enhanced embryonic lethality [(Hariri et al., 2023); Figure S1B]. The C-terminal HSR-9::GFP::3xHA fusion in combination with *brc-1* showed similar embryonic lethality to the *hsr-9; brc-1* double mutant, suggesting it is nonfunctional. On the other hand, *gfp::v5::hsr-9; brc-1* double mutant exhibited embryonic lethality at levels between that of wild type and *hsr-9; brc-1,* suggesting that GFP::V5::HSR-9 is partially functional (Figure S1C). Both fusions showed similar localization in the *C. elegans* germ line (Figure 1C and Figure S1C). We subsequently concentrated our localization studies on worms expressing the GFP::V5::HSR-9 fusion.

We monitored HSR-9 localization by live imaging focusing on the *C. elegans* germ line, which contains proliferating germ cells at the distal end and all stages of meiotic prophase arranged in a spatial-temporal gradient towards the proximal end (Figure 1C). Consistent with a previous study using an antibody directed against HSR-9 (Ryu et al., 2013), GFP fluorescence was enriched in the nucleus of proliferating germ

cells (Figure 1C). In metaphase and anaphase of mitosis, where the nuclear envelope breaks down and chromosomes condense, HSR-9 was localized to the condensed chromosomes (PZ, arrows; Figure 1C), suggesting that the protein is chromatin-associated. In meiotic germ cells, HSR-9 was observed on chromatin throughout prophase, first appearing in tracks as chromosomes synapse, and subsequently on condensed chromosomes in diplotene/diakinesis (Figure 1C).

In contrast to observations from live imaging, the GFP::V5::HSR-9 signal in dissected and fixed gonads did not show as tight an association with chromatin (Ryu et al., 2013). This pattern held true regardless of whether we used antibodies directed against GFP or V5, or imaged GFP fluorescence directly on samples prepared by dissection in paraformaldehyde followed by ethanol fixation. Rapid freeze crack and fixation in cold ethanol followed by paraformaldehyde treatment of dissected gonads more closely but not entirely recapitulated the results by live imaging (Figure 1D). As proteins containing intrinsically disordered regions have been shown to have different localization patterns in fixed versus live cells, the difference we observed for HSR-9 localization is likely a consequence of rapid association/disassociation of HSR-9 with chromatin (Irgen-Gioro et al., 2022; Schmiedeberg et al., 2009; Teves et al., 2016).

HSR-9 is enriched on the *X* chromosome pair in hermaphrodite germ cells

We noted that GFP::V5::HSR-9 fluorescence in live hermaphrodite worms was more intense in two nuclear domains in many mitotic germ cells where homologous chromosomes are unpaired, and on one chromosome track in pachytene germ cells where homologous chromosomes are paired and synapsed (asterisks, Figure 1C). We

hypothesized that the GFP::V5::HSR-9-enriched regions were the *X* chromosomes, which have different chromatin properties compared to the autosomes (Bean et al., 2004; Checchi & Engebrecht, 2011; Jaramillo-Lambert & Engebrecht, 2010; Kelly et al., 2002; Reuben & Lin, 2002). To test this, we imaged live worms expressing mCherry::HIM-8, the *X* chromosome-specific pairing center protein (Link et al., 2018; Phillips et al., 2005), and found that mCherry::HIM-8 labelled the two GFP::V5::HSR-9 enriched domains in many proliferating germ cells as well as the single chromosome track enriched for GFP::V5::HSR-9 in pachytene germ cells (Figure 2A). This result is consistent with GFP::V5::HSR-9 being concentrated on *X* chromosomes. Interestingly, while we observed a single HIM-8-associated GFP::V5::HSR-9 enriched region in mitotic germ cells in the male germ line, consistent with enrichment on the single *X* chromosome of males, we did not observe enrichment on the *X* chromosome in male pachytene germ cells (Figure 2B). Thus, GFP::V5::HSR-9 is associated with chromatin, and is enriched on the *X* chromosome(s) in both oogenic and spermatogenic proliferating germ cells but only on the *X* chromosome pair in oogenic pachytene germ cells.

Mammalian 53BP1 associates with histone H4 dimethylated on lysine 20 (H4K20me2). In *C. elegans* pachytene germ cells, H4K20me1 is enriched on autosomes relative to the *X* chromosomes due to autosomal targeting of the DPY-21 demethylase, which converts H4K20me2 to H4K20me1 (Brejc et al., 2017; Vielle et al., 2012). This suggests that *X* chromosomes are enriched for H4K20me2/3 and this enrichment may contribute to HSR-9 accumulation on the *X* chromosomes. As we were unable to identify antibodies specific for H4K20me2/3, we labelled germ lines with

antibodies against H4K20me1 and observed enrichment on autosomes relative to the *X* chromosomes as previously reported (Brejc et al., 2017; Vielle et al., 2012) (Figure 2C). We next examined the immunolocalization of H4K20me1 in two different deletion mutants of the SET-4 methyltransferase, which adds methyl groups to H4K20me1 to generate H4K20me2 and H4K20me3 (Kramer et al., 2015; Vielle et al., 2012; Wells et al., 2012). *set-4(ok1481)* contains a 913bp C-terminal deletion that removes that last 17 amino acids and 3'UTR, while *set-4(n4600*) contains a 1146bp deletion that removes upstream sequences and the first 165 of 288 amino acids. In both mutants, H4K20me1 was detectable on the *X* chromosome pair, consistent with the *X* chromosomes being enriched for SET-4-dependent H4K20me2/me3 in wild-type animals (Figure 2C). Analysis of GFP::V5::HSR-9 in *set-4* mutants revealed a reduced, but still detectable, enrichment of GFP::V5::HSR-9 on the *X* chromosome pair (Figure 2D, E). These results suggest that H4K20me2/me3 contributes to the enrichment of HSR-9 on the *X* chromosome pair, but there are additional factors, likely including other chromatin marks, that influence HSR-9 recruitment.

HSR-9 localizes to kinetochores but does not play an essential role in monitoring kinetochore-spindle attachments/tension

In mammalian somatic cells, 53BP1 accumulates at kinetochores and centrosomes in addition to being associated with chromatin (Jullien et al., 2002; Yim et al., 2017). *C. elegans* chromosomes are holocentric, with kinetochore proteins binding along the poleward face of each sister chromatid during mitosis and forming cup-shaped structures on meiotic chromosomes (Albertson & Thomson, 1982; Monen et al., 2005).

While no centrosome localization was detected, we observed GFP::V5::HSR-9 in bar-like structures on the poleward face of metaphase chromosomes in proliferating germ cells and in embryos (Figure 3A). To confirm that GFP::V5::HSR-9 is enriched on kinetochores, we performed immunolabeling with antibodies against the kinetochore-associated CENP-A ortholog, HCP-3 (Gassmann et al., 2012) and imaged GFP fluorescence. We observed both HCP-3 and GFP fluorescence in bar-like structures that co-localized on the poleward face of metaphase chromosomes in proliferating germ cells (Figure 3B), confirming that HSR-9 is enriched at kinetochores. GFP::V5::HSR-9 was also observed surrounding the outer edge of chromosomes at the -1 oocyte and at the meiotic divisions (Figure 3A), consistent with kinetochore localization.

Mammalian 53BP1 at the kinetochore has been shown to play a role in monitoring inappropriate microtubule attachments or tension (Jullien et al., 2002; Wang et al., 2017). To determine whether HSR-9 plays a similar role in germ cells, we disrupted metaphase using the *zyg-1(b1)* conditional mutant [referred to as *zyg-1(ts)*; (O'Connell et al., 2001; Wood et al., 1980)], which we previously showed perturbed spindle function in mitotically-dividing germ cells and activated the DNA damage response and spindle assembly checkpoint (Lawrence et al., 2015). ZYG-1 is functionally related to PLK4 and is required for centrosome duplication (O'Connell et al., 2001). Its inactivation leads to the formation of monopolar spindles and disrupts spindle attachments and tension. This results in a cell cycle delay, which is evidenced by an increase in the number of nuclei enriched for phosphorylation of Serine 10 on Histone H3 (H3S10P), a marker of prometaphase/metaphase (Lawrence et al., 2015; Prigent & Dimitrov, 2003). As expected, we observed an increase in H3S10P-positive nuclei

following ZYG-1 inactivation at 25°C, indicative of a metaphase delay (Figure 3C, D). Inactivation of *zyg-1(ts)* at the nonpermissive temperature in the *hsr-9(xoe17)* mutant did not alter the number of H3S10P-positive nuclei, suggesting that HSR-9 is not required for monitoring microtubule attachment/tension and checkpoint activation in the *zyg-1(ts)* mutant (Figure 3C, D). We also examined the consequence of HSR-9 mutation on progeny viability at different temperatures in the *zyg-1(ts)* mutant. No enhancement of progeny lethality was observed in the absence of HSR-9, consistent with our findings that HSR-9 is not essential for cell cycle delay when monopolar spindles are induced. Thus, HSR-9 is enriched at kinetochores in metaphase but does not play a significant role in monitoring spindle attachments/tension at kinetochores in *C. elegans*.

HSR-9 regulates meiotic DSB processing

In somatic cells, 53BP1 functions in the DNA damage response and repair choice (Mirman & de Lange, 2020). Further, 53BP1 becomes enriched in nuclear foci following DNA damage, and has been widely used as a marker of DSBs (Ward, Minn, Jorda, et al., 2003). No obvious GFP::V5::HSR-9 foci were observed in meiotic cells, where DSBs are induced by SPO-11 (Figure 1C). Further, no GFP::V5::HSR-9 foci were observed following irradiation (IR) treatment, suggesting that HSR-9 does not accumulate at DSBs in *C. elegans* germ cells (Ryu et al., 2013) (Figure 4A).

While HSR-9 does not accumulate at DSBs, HSR-9 has been reported to play a role in repair of IR-induced breaks in the germ line when HR is impaired (Ryu et al., 2013). To determine whether HSR-9 functions in repair of meiotic DSBs, we analyzed

meiotic recombination in *hsr-9(xoe17)* and the previously described *hsr-9(ok759)* allele, which removes 1613 bps in the middle of the gene (Ryu et al., 2013) (Figure S1A). Progeny viability was high (Figure S1B) and there was no increase in male self-progeny in either *hsr-9(ok759)* or *hsr-9(xoe17)* mutants (wt = 0.02±0.01, *hsr-9(ok759)* = 0.01±0.05, *hsr-9(xoe17)* = 0.01±0.04% males), suggesting that HSR-9 is not essential for meiotic recombination. Further, blocking apoptosis by mutation of CED-3, the caspase essential for executing cell death (Ellis & Horvitz, 1986; Yuan et al., 1993), did not increase the number of inviable progeny compared to the *ced-3* mutant alone, suggesting that the lack of elevated progeny lethality is not due to culling by apoptosis in the absence of HSR-9 (Figure S2A).

Meiotic DSBs are catalyzed by the conserved topoisomerase SPO-11 (Bergerat et al., 1997; Dernburg et al., 1998; Keeney et al., 1997), and then processed for repair predominately by HR. We monitored meiotic DSB repair by examining the appearance and disappearance of the Replication Protein A (RPA) complex and RAD-51 in the spatiotemporal organization of the *C. elegans* germ line. RPA coats single-stranded DNA generated by end resection. In *C. elegans*, RPA is composed of RPA-1 and RPA-2 (Hefel et al., 2021) and GFP::RPA-1 is observed in foci from early prophase (leptotene/zygotene) through pachytene, suggesting that it not only marks resected ends but also recombination intermediates post-resection (Woglar & Villeneuve, 2018). In live worms, GFP::RPA-1 is nucleoplasmic with some nuclear foci visible (Li et al., 2020; Li et al., 2023). Live cell imaging of GFP::RPA-1 in wild type and *hsr-9(xoe17)* revealed more intense foci in the *hsr-9(xoe17)* mutant (Figure 4B). To quantify this, we measured the coefficient of variation (CV), which describes the dispersion of pixel

intensity values from a 2D region of interest around the mean pixel intensity such that nuclei with more foci above the nucleoplasmic signal will have high CV values, whereas nuclei with more uniform fluorescence will have low CV values (Bishop et al., 2015). We observed a higher CV of GFP::RPA-1 in *hsr-9(xoe17)* compared to wild type in both leptotene/zygotene and pachytene nuclei (Figure 4C). GFP::RPA-1 fluorescence also had a higher CV in the *hsr-9(ok759)* mutant (Figure S2B).

We next examined the assembly and disassembly of RAD-51 (Rinaldo et al., 2002) in the presence and absence of HSR-9 using antibodies against RAD-51 (Alpi et al., 2003; Colaiacovo et al., 2003). RAD-51 replaces the RPA complex on resected DSBs beginning in leptotene/zygotene (transition zone) and is largely removed by late pachytene (Colaiacovo et al., 2003). While the overall pattern of RAD-51 is similar in *hsr-9* mutant vs. wild-type germ lines, there was a significant increase in the number of RAD-51 foci detected in early meiotic prophase (transition zone and early pachytene) in both *hsr-9(xoe17)* and *hsr-9(ok759)* mutants (Figure 4D, E; Figure S2C). Elevated RPA-1 and RAD-51 foci could be a consequence of a greater number of DSBs repaired by HR, and/or a defect in processing of DSBs.

To provide insight into the nature of the elevated RAD-51 foci in *hsr-9* mutants, we analyzed RAD-51 in the absence of RAD-54. *rad-54* mutants have been used to distinguish between increased number of DSBs vs. a defect in processing of breaks as RAD-54 is essential for RAD-51-mediated strand exchange during HR and is required for RAD-51 disassembly; in its absence RAD-51 remains on processed breaks (Mets & Meyer, 2009; Solinger et al., 2002). The number of RAD-51 foci per nucleus in *rad-54* mutants in the presence or absence of HSR-9 was not statistically different (Figure 4F,

413 G and Figure S2D), suggesting that HSR-9 does not alter the number of DSBs formed
414 but rather regulates the processing of DSBs by HR.
415
416 **Not all crossovers accumulate COSA-1 in the absence of HSR-9**
417 To determine whether the defect in processing of DSBs alters crossovers in the *hsr-9*
418 mutants, we monitored the crossover site associated protein COSA-1/CNTD1 (Yokoo et
419 al., 2012). Wild-type hermaphrodites have six GFP::COSA-1 foci per nucleus, one on
420 each of the six pairs of homologous chromosomes, in mid-late pachytene. In *hsr-9*
421 mutants, while the average remained six, we observed ~9% of nuclei containing only
422 five GFP::COSA-1 foci (Figure 5A, B). These results suggest that HSR-9 regulates the
423 processing of DSBs into COSA-1-marked events.
424 Given HSR-9's enrichment on *X* chromosomes (Figure 2), we examined whether
425 those nuclei containing five COSA-1 foci were lacking GFP::COSA-1 on the *X*
426 chromosome pair. To that end, we labelled chromosomes with antibodies directed
427 against the synaptonemal complex central region component SYP-1 (MacQueen et al.,
428 2002) in worms expressing both GFP::COSA-1 and mCherry::HIM-8. Among nuclei with
429 five GFP::COSA-1 foci, where mCherry::HIM-8 could be detected, 17.4 % (4/23) lacked
430 a GFP::COSA-1 on the *X* chromosome pair (Figure 5C). If all six chromosome pairs
431 have an equal probability of not receiving a COSA-1 focus, 16.7% nuclei are predicted
432 to lack a GFP::COSA-1 foci on the *X* chromosome pair. Thus, the lack of a COSA-1
433 focus in nuclei containing five foci is not limited to the *X* chromosome pair in the *hsr-9*
434 mutant.

435 The reduction in COSA-1 foci in *hsr-9* mutants was surprising given the high
436 progeny viability and suggests that COSA-1 may not mark all crossovers in the absence
437 of HSR-9. To determine whether the alteration in GFP::COSA-1 foci reflects changes in
438 genetic crossovers, we monitored genetic linkage between SNP markers on
439 chromosomes *I* and *V* in Bristol/Hawaiian hybrid strains (Figure 5D). There was no
440 statistical difference between the genetic map distances in wild type and *hsr-9* for either
441 chromosome *I* or *V* (*I*: WT = 45.1cM; *hsr-9(xoe17)* = 50.39cM; *V*: WT= 47.36; *hsr-*
442 *9(xoe17)* = 40.86cM; Figure 5D, File S4), suggesting that genetic crossover numbers
443 are not altered in the absence of HSR-9. Alternatively, genetic SNP mapping is not
444 sensitive enough to detect subtle changes in crossover numbers distributed throughout
445 the genome.

446 In *C. elegans*, crossovers are not evenly distributed along the length of the
447 chromosomes but are enriched on the gene-poor arms and many meiotic mutants alter
448 crossover distribution (Barnes et al., 1995; Lim et al., 2008; Rockman & Kruglyak, 2009).
449 Analysis of crossover distribution revealed that mutation of *HSR-9* had little effect, except
450 in the middle of chromosome *V* where there were statistically more crossovers in the left-
451 center compared to wild-type hermaphrodites (2.77% vs.14.13%; p=0.0405; Table S4,
452 Figure 5D). Together, these results suggest that HSR-9 does not alter crossover numbers
453 but plays a role in promoting COSA-1 accumulation at a subset of recombination events.
454

455 **HSR-9 in meiotic checkpoint signaling**

456 To determine whether HSR-9 functions in meiotic checkpoint signaling we analyzed the
457 consequence of removing HSR-9 in mutants defective in crossover recombination

458 leading to activation of the recombination checkpoint (Gartner & Engebrecht, 2022). To
459 that end, we constructed *hsr-9(xoe17); zim-2(tm574)* and *hsr-9(xoe17); him-8(me4)*
460 double mutants and analyzed progeny viability, male self-progeny, checkpoint signaling,
461 and apoptosis. ZIM-2 binds to the chromosome *V* pairing center, while HIM-8 binds to
462 the *X* chromosome pairing center. In *zim-2* or *him-8* mutants, chromosome *Vs* or *X*
463 chromosomes fail to pair, synapse, and form crossovers, leading to elevated embryonic
464 lethality or male progeny, respectively (Phillips & Dernburg, 2006; Phillips et al., 2005).
465 Embryonic lethality was similar in *zim-2(tm574)* and the *hsr-9(xoe17); zim-2(tm574)*
466 double mutant as well as in *him-8(me4)* and *hsr-9(xoe17); him-8(me4)* (Figure 6A).
467 Surprisingly, we observed fewer males in *hsr-9(xoe17); him-8(me4)* compared to *him-*
468 *8(me4)* (Figure 6B). A reduction in the number of males was also observed in *hsr-*
469 *9(xoe17); him-8(tm611)*; *him-8(tm611)* is a deletion allele, and *hsr-9(ok759); him-*
470 *8(me4)* mutants, suggesting the phenotype is not allele-specific (Figure 6B). We next
471 examined checkpoint signaling by immunolabeling with an antibody that recognizes Ser
472 345 phosphorylation of the checkpoint kinase CHK-1, which is phosphorylated in
473 response to checkpoint activation and is dependent on ATR (Jaramillo-Lambert et al.,
474 2010). Similar levels of Ser345p, as indicated by the number of pCHK-1 foci per
475 nucleus, were observed both in the presence and absence of HSR-9 in the *him-8*
476 mutant background, suggesting that HSR-9 does not influence checkpoint activation in
477 response to unpaired chromosomes and their failure to establish a crossover (Figure
478 6C, D). On the other hand, apoptosis was reduced in the absence of HSR-9, consistent
479 with what was observed in response to IR (Figure 6E) (Ryu et al., 2013).

To determine the nature of the defect in production of male self-progeny, we first examined whether HSR-9 plays a role in *X* chromosome pairing by monitoring mCherry::HIM-8 in the presence and absence of HSR-9. As previously reported, in wild-type hermaphrodites, pairing of *X* chromosomes is initiated at the leptotene/zygotene (transition zone) stage of meiosis (Phillips et al., 2005). By early pachytene, stable association of HIM-8 signals was achieved in nearly 100 percent of nuclei (Figure 7A). The same pattern was observed in *hsr-9(xoe17)* mutants (Figure 7A). Thus, it is unlikely that an earlier defect in pairing is altering *X* chromosome segregation.

We next monitored oocyte chromosome nondisjunction by constructing strains containing X-linked GFP and tdTomato nuclear markers (El Mouridi et al., 2022). Hybrid strains expressing both green and red nuclear fluorescence were crossed to males carrying the *X*-linked *lon-2* mutation, allowing us to distinguish two types of non-disjunction events: oocytes containing no *X* chromosome (nullo X) fertilized by *lon-2* male sperm resulting in long males and *XX* oocytes fertilized by male sperm leading to worms expressing both nuclear GFP and tdTomato. As expected, we observed approximately equal numbers of green and red progeny from wild type and *hsr-9(xoe17)* mutants (wt: 52.5±4.4 green, 47.5±4.4 red; *hsr-9(xoe17)*: 54.4±4.0 green, 45.6±4.0 red), and recorded no nondisjunction events (Figure 7B). In *him-8(tm611)* we observed ~38% nondisjunction events composed of 24.2±6.0% nullo *X* and 13.8±2.8 *XX* oocytes. In *hsr-9(xoe17); him-8(tm611)* we observed significantly fewer nondisjunction events (~19%; $p>0.02$) of which 10.5±2.1% were nullo *X* and 8.5±3.9% were *XX* oocytes (Figure 7B). Thus, HSR-9 influences the segregation pattern of the *X* chromosomes in oocytes when their pairing, synapsis, and recombination are disrupted.

Given the role of HSR-9 in *X* chromosome segregation in the *him-8* mutant background and the enrichment of GFP::V5::HSR-9 on the *X* chromosome pair, we monitored the localization of GFP::V5::HSR-9 in the *him-8* mutant. We observed enrichment on two chromosome domains in many proliferative germ cells, as with wild type. In meiosis, many nuclei had regions with more intense fluorescence, consistent with enrichment on the unpaired *X*s, but as we could not label the *X* chromosomes (with mCherry::HIM-8 or via methods that require fixation), we could not definitively conclude these were the *X* chromosomes (Figure 7C). To gain further insight, we asked if the GFP::V5::HSR-9 enrichment was a consequence of the pairing status of the *X* chromosomes in meiosis. To that end, we examined localization of GFP::V5::HSR-9 in the *tra-2* loss-of-function mutant, which transforms *XX* animals into males (Hodgkin & Brenner, 1977). While GFP::V5::HSR-9 fluorescence was enriched on the *X*s as marked by mCherry::HIM-8 in proliferating germ cells, no enrichment was observed in meiotic cells similar to wild-type males containing a single *X* chromosome (Figure 7C). These results suggest that it is not the pairing status *per se* that leads to accumulation of GFP::V5::HSR-9 on the *X* chromosomes in oogenic germ cells.

Discussion

We show here that HSR-9, the *C. elegans* 53BP1 homolog, is chromatin-associated, enriched on the *X* chromosome pair in oogenic germ cells, and on kinetochores at metaphase of mitosis and meiosis. Mutant analysis revealed a subtle role for HSR-9 in meiotic DSB processing, checkpoint signaling, and a previously unrecognized role in *X* chromosome segregation when X chromosomes fail to pair, synapse, and recombine.

HSR-9 is associated with a unique chromatin state

As in mammals, HSR-9 is chromatin-associated and becomes enriched on kinetochores in dividing cells, suggesting that HSR-9 associates with a particular chromatin state. However, in contrast to mammals where 53BP1 marks DSBs in association with γ-H2AX, HSR-9 does not become enriched at either meiotic or IR-induced breaks (Figures 1 and 4A). Further, no γ-H2AX variant has been identified in *C. elegans*. In many organisms, meiotic DSBs occur at hotspots, special chromosomal sites dictated largely by the chromatin state (Tock & Henderson, 2018); however, this does not appear to be the case in *C. elegans* (Bernstein & Rockman, 2016; Kaur & Rockman, 2014). Instead, DSBs (and crossovers) are enriched on chromosome arms, which have a distinct chromatin landscape compared to the middle of the chromosomes (Lascarez-Lagunas et al., 2023). The pattern of DSBs observed may be a consequence of the holocentric nature of *C. elegans* chromosomes (Altendorfer et al., 2020). Together, these results suggest that *C. elegans* has a unique, but as yet undefined, chromatin state at DSBs sites, which does not include enrichment of HSR-9.

Although it is not enriched at DSBs, HSR-9 is enriched on *X* chromosome(s) in spermatogenic and oogenic proliferating germ cells but only the *X* chromosome pair in meiotic prophase oocytes (Figure 2). We provide evidence that HSR-9 interacts with H4K20me2/3 as 53BP1 does in mammals. However, this interaction contributes, but is not essential for, its enrichment on the *X* chromosome pair. 53BP1 has also been shown to interact with H2AK15ub (Fradet-Turcotte et al., 2013; Wilson et al., 2016), although there is no evidence that this chromatin modification is present in *C. elegans*. Thus, it is likely that HSR-9 associates with a distinct chromatin state. We do show that

549 HSR-9, like 53BP1, has a highly disordered N-terminus, and based on results from
550 different fixation conditions, is likely to interact dynamically with chromatin. Further, our
551 findings that HSR-9 enrichment is specific to the *X* chromosomes in oogenic meiosis but
552 not in male meiosis, are also consistent with its association with a unique chromatin
553 state. That GFP::V5::HSR-9 is not enriched on the paired *X* chromosomes in male germ
554 cells in the sex determination mutant *tra-2*, which transforms *XX* worms into males,
555 suggests that the difference is not due to the pairing status of the *X*. This is also
556 consistent with our previous findings that the *X* of males has distinct chromatin
557 properties from the *X* chromosome pair in oogenesis independent of pairing status
558 (Checchi & Engebrecht, 2011).
559
560 ***The role of HSR-9 in meiotic recombination***
561 53BP1 orthologs have been shown to function in both early and late processing of
562 DSBs. In somatic cells, 53BP1 plays an early role in repair choice through its interaction
563 with RIF1, the Shieldin complex, and PTIP to bind at DSBs and block resection, thereby
564 promoting NHEJ (Chapman et al., 2013; Escribano-Diaz et al., 2013; Mirman et al.,
565 2018; Noordermeer et al., 2018). 53BP1 has also been suggested to play later roles in
566 both limiting RAD51 loading and stimulating strand annealing for repair by HR (Callen et
567 al., 2020; Ferrari et al., 2020). We find that HSR-9 plays a role in meiotic DSB repair as
568 shown by elevated levels of both RPA-1 and RAD-51 (Figure 4). This is unlikely due to
569 a defect in repair choice, as blocking RAD-51 at DSBs by mutation of RAD-54 does not
570 alter the number of RAD-51 foci, suggesting that the same number of DSBs are
571 processed by HR in the *hsr-9* mutant compared to wild type. Interestingly, we find that

572 although there appears to be a delay in the processing of DSBs in the *hsr-9* mutant,
573 there is no effect on progeny viability suggesting that DSBs are properly repaired and
574 establish crossovers for accurate chromosome segregation. A small subset of DSBs is
575 processed into crossovers without accumulating COSA-1, suggesting that either COSA-
576 1 is not required for a subset of crossovers, or more likely, that COSA-1 is required but
577 does not accumulate to cytological visible levels in the absence of HSR-9 as suggested
578 by Yokoo et al. (Yokoo et al., 2012). Whether this is a consequence of direct
579 interactions between HSR-9 and DSB processing machinery, and/or an indirect effect of
580 the chromatin state requires further investigation.
581
582 **Checkpoint signaling and sex chromosomes**
583 In yeast, Rad9, the 53BP1 homolog, was the first checkpoint protein to be discovered
584 and subsequent analyses of mammalian 53BP1 was consistent with a role in checkpoint
585 signaling (Schultz et al., 2000; Weinert & Hartwell, 1989). Our study suggests that HSR-
586 9 plays a subtle role in DNA damage checkpoint signaling. We found that in the
587 absence of HSR-9, the checkpoint kinase, CHK-1, is phosphorylated in response to
588 defects in chromosome pairing, synapsis, and recombination, suggesting that detection
589 and relay through the checkpoint pathway is not perturbed. However, checkpoint-
590 dependent apoptosis is diminished in the absence of HSR-9 as was previously shown in
591 response to IR-induced DNA breaks (Ryu et al., 2013). Further, we did not uncover a
592 checkpoint role for HSR-9 in response to unattached kinetochores even though HSR-9
593 is enriched at kinetochores. In contrast, mammalian 53BP1 has been shown to be both

enriched at kinetochores and to monitor spindle attachments/tension (Jullien et al., 2002; Wang et al., 2017; Yim et al., 2017).

Although apoptosis is impaired when both autosomes and sex chromosomes are unable to pair, synapse and recombine, we discovered a reduction in male self-progeny in *hsr-9* mutants when sex chromosome pairing, synapsis and recombination are impaired. Analysis of chromosome nondisjunction events in oogenesis suggests that HSR-9 influences the pattern of *X* chromosome segregation under these conditions. Perhaps HSR-9 enrichment on the *X* chromosomes alters how the unattached *X* chromosomes align and segregate during meiosis I, leading to a higher likelihood of generating nullo *X* gametes for production of males.

Conclusion. 53BP1 regulates several aspects of chromosome biology – presumably through its chromatin association. There appears to be both commonalities and unique properties of 53BP1 homologs across evolution and these differences may reflect different chromatin environments in different organisms. In worms, its concentration on the *X* chromosomes suggests that HSR-9 plays a role in influencing *X* chromosome segregation in addition to its role in DSB processing.

Acknowledgements

We thank the Engebrecht laboratory for thoughtful discussions. We also acknowledge the Caenorhabditis Genetic Center, which is funded by the National Institutes of Health (NIH) Office of Research Infrastructure Programs (P40 OD010440) for providing

strains. This work was supported by NIH GM103860 and GM103860S1 to J.E. EH was supported by the UC Davis OEOES Research Fellowship Program.

Data availability

Strains and reagents are available upon request. The authors affirm that all data necessary for confirming the conclusions of this article are represented fully within the article and its tables and figures. Supplemental material available at Figshare. Table S1 contains *C. elegans* strain information; Table S2 contains CRISPR information; Table S3 contains antibody information and File S4 contains the raw meiotic mapping data. Figure S1 shows *hsr-9* gene structure, embryonic lethality of mutants and fusions, and localization of HSR-9::GFP::3xHA. Figure S2 shows the consequence of blocking apoptosis to *hsr-9* progeny viability, recombination analyses of the *hsr-9(ok759)*, and full gonad images of RAD-51 labelling.

Figure legends

Figure 1. HSR-9 is a chromatin-associated protein with intrinsically disordered N-terminal region. A) Predicted structure of HSR-9 determined by AlphaFold (Jumper et al., 2021). N-terminus is indicated in brown line. B) Predicted disordered regions of HSR-9 using IUPred3 (Erdos et al., 2021). C) Images of GFP::V5::HSR-9 fluorescence from indicated regions of the germ line. Red arrows mark condensing chromosomes in prometaphase to anaphase, asterisks mark two domains with stronger fluorescense intensity. PZ = proliferative zone; TZ = transition zone; EP = early pachytene; MP = mid pachytene; LP = late pachytene; DP = diplotene; DK = diakinesis. Scale bar = 10μm. D)

639 Images of GFP::V5::HSR-9 fluorescence of the pachytene region of dissected gonads
640 following rapid freeze crack, fixation in cold ethanol and paraformaldehyde treatment
641 counterstained with DAPI. Scale bar = 10μm.
642
643 **Figure 2. GFP::V5::HSR-9 is enriched on *X* chromosomes in oogenesis and**
644 **associates with H4K20me2/me3.** Images of GFP::V5::HSR-9 (grey) and
645 mCherry::HIM-8 (magenta) from mitotic (PZ, proliferative zone) and meiotic (MP, mid-
646 pachytene) regions of the germ line in live A) hermaphrodites and B) males. C) Images
647 of fixed and dissected meiotic germ cells labelled with antibodies against H4K20me1
648 (cyan) in wild type and *set-4(ok1481)* expressing mCherry::HIM-8 (magenta) and
649 counter-stained with DAPI (grey). Arrows point to the X chromosomes. Scale bar =
650 5μm. D) GFP::V5::HSR-9 fluorescence of whole gonads from live worms from wild type,
651 *set-4(ok1481)*, and *set-4(n4600).* Scale bar = 20 μm. E) Quantification of the relative
652 fluorescence intensity of the *X* to autosome ratio (n=3 worms for each genotype). *** p <
653 0.001; ** p < 0.01 by Mann-Whitney.
654
655 **Figure 3. GFP::V5::HSR-9 is enriched on kinetochores but doesn't play an**
656 **essential role in monitoring microtubule-kinetochore attachments.** A) Live imaging
657 of GFP::V5::HSR-9 fluorescence in mitotic germ cells, -1 diakinesis oocyte, Meiosis I
658 fertilized oocyte and embryo showing structures consistent with enrichment on
659 kinetochores. B) Fixed images of mitotic germ cells labelled with CENPA ortholog, HCP-
660 3 (magenta) and direct GFP fluorescence (cyan). Scale bar = 5μm. C) Fixed images of
661 mitotic region of germ line labelled with antibodies directed against H3S10P and

662 counterstained with DAPI at indicated temperatures. Scale bar = 20 μm. D)
663 Quantification of H3S10P nuclei/germ line in *zyg-1(ts)* and *hsr-9(xoe17); zyg-1(ts)*
664 grown at 15° or 25°C. Number of germ lines examined: *zyg-1(ts)* 15°C = 21; *zyg-1(ts)*
665 25°C = 21; hsr-9(xoe17); *zyg-1(ts)* 15°C = 21; *hsr-9(xoe17); zyg-1(ts)* 15°C = 22; ** p <
666 0.01; by Mann-Whitney. E) % embryonic lethality of *zyg-1(ts)* and *hsr-9(xoe17); zyg-*
667 *1(ts)*; 6 worms were examined at each temperature.
668
669 **Figure 4. HSR-9 plays a role in processing of meiotic DSBs.** A) Images of
670 GFP::V5::HSR-9 fluorescence from indicated regions of the germ line 1hr post 75Gys
671 IR. PZ = proliferative zone; TZ = transition zone; EP = early pachytene; MP = mid
672 pachytene; LP = late pachytene; DP = diplotene; DK = diakinesis. Scale bar = 10μm. B)
673 GFP-RPA-1 fluorescence in leptotene/zygotene and pachytene. Scale bar = 5μm. C)
674 Coefficient of Variation (CV) of GFP::RPA-1 fluorescence was measured from 3 germ
675 lines. Images of early pachytene nuclei immunolabelled with RAD-51 (red) and counter
676 stained with DAPI (blue) from wild type (WT) and *hsr-9(xoe17)* germ lines (D) and
677 corresponding quantification (E), and *rad-54(ok615)* and *hsr-9(xoe17); rad-54(ok615)*
678 (F) and corresponding quantification (G). Box whisker plots show number of RAD-51
679 foci per nucleus in the indicated regions. Horizontal line of each box represents the
680 median, top and bottom of each box represent medians of upper and lower quartiles,
681 lines extending above and below boxes indicate SD, and individual data points are
682 outliers from 5 to 95%. Statistically significant comparisons by Mann–Whitney of WT vs.
683 *hsr-9(xoe17)* are indicated; ***p< 0.0001. Complete germlines are shown in Figure S2.

Figure 5. Reduced numbers of GFP::COSA-1, but not genetic crossovers in the absence of HSR-9. A) Percent of nuclei containing indicated GFP::COSA-1 foci in *gfp::cosa-1(xoe44)* and *hsr-9(xoe17); gfp::cosa-1(xoe44),* which is at the endogenous locus on chromosome *III* and *meIs8[unc-119(+) pie-1promoter::gfp::cosa-1]* and *hsr-9(ok759); meIs8[unc-119(+) pie-1promoter::gfp::cosa-1]* inserted on chromosome *II*. B) Image of mid-late pachytene nuclei showing GFP::COSA-1(green) and counterstained with DAPI (blue). Number of GFP::COSA-1 foci are indicated on each nucleus. Scale bar = 5µm. C) Images of pachytene nuclei immunolabelled with SYP-1 antibodies (blue), and imaged for mCherry::HIM-8 (magenta) and GFP::COSA-1 (green) fluorescence. Scale bar = 1 µm. D) Top: SNP markers (red) on Chromosome *I* and *V*. Middle: crossover frequency on Chromosomes *I* and *V*. Bottom: crossover distribution among recombinants on Chromosomes *I* and *V*. Total number of worms analyzed for Chromosome *I* markers = wild type (n = 184), and *hsr-9(xoe17)* (n = 367); Chromosome *V* markers = wild type (n = 228), and *hsr-9(xoe17)* (n = 230). Statistical analyses were conducted using $\chi 2$ on 2-by-2 contingency tables,* $p<0.05$.

Figure 6. Apoptosis is reduced but checkpoint signaling appears intact in *hsr-9* mutants. A) Embryonic lethality in *zim-2(tm574)*, *hsr-9(xoe17); zim-2(tm574)*, *him-8(me4)* and *hsr-9(xoe17); him-8(me4)* mutants (n=10). B) % male self-progeny in him-8(me4), *hsr-9(xoe17); him-8(me4), hsr-9(ok759); him-8(me4), hsr-9(xoe17); him-8(tm611)* and *him-8(tm611)* mutants (n=10). C) Early pachytene germ cells immunolabelled with CHK-1Ser345p (green) in WT, *hsr-9(xoe17)*, *him-8(me4)* and *hsr-9(xoe17); him-8(me4)*. Scale bar = 5µm. D) Number of CHK-1Ser345p foci per nuclei in

WT (n=187), *hsr-9(xoe17)* (n=200), *him-8(me4)* (n=75) and *hsr-9(xoe17); him-8(me4)* n=87). E) Number of apoptotic nuclei/gonad by Acridine Orange staining in WT (n=44), *hsr-9(xoe17)* (n=45) *zim-2(tm574)* (n=41), *hsr-9(xoe17); zim-2(tm574)* (n=24), *him-8(me4)* (n=26) and *hsr-9(xoe17); him-8(me4)* (n=32). * p<0.05; ** p<0.001; *** p<0.0001 by Mann-Whitney.

Figure 7. HSR-9 plays a role in *X* chromosome segregation in *him-8*. A) % nuclei with paired (1 focus) mCherry::HIM-8 foci in *mCherry::him-8* and *hsr-9(xoe17); mCherry::him-8* worms at the indicated stages of meiotic prophase: PZ, proliferative zone, TZ, transition zone; EP, early pachytene; MP, mid pachytene. Three gonads were analyzed for each genotype. B) % oocytes with *X* chromosome expressing GFP::2xNLS (green), tdTomato::H2B (red), both GFP::2xNLS and tdTomato::H2B (*XX* - yellow) or no *X* chromosome (nullo-*X* - grey). Number of progeny examined: WT = 148, *hsr-9(xoe17)* = 196, *him-8(tm611)* = 145, *hsr-9(xoe17); him-8(tm611)* = 163. * p<0.05 by $\chi 2$ on 2-by-4 contingency tables C) Images of GFP::V5::HSR-9 (grey) in *him-8* (yellow asterisks denote regions of more intense fluorescence) and GFP::V5::HSR-9 (grey) and mCherry::HIM-8 (magenta) in *tra-2 XX* males from mitotic and meiotic regions of the germ line in live worms. Scale bar = 5μm.

Literature cited

Albertson, D. G., & Thomson, J. N. (1982). The kinetochores of Caenorhabditis elegans. *Chromosoma*, *86*(3), 409-428. https://doi.org/10.1007/BF00292267

Alpi, A., Pasierbek, P., Gartner, A., & Loidl, J. (2003). Genetic and cytological characterization of the recombination protein RAD-51 in Caenorhabditis elegans. *Chromosoma*, *112*(1), 6-16. https://doi.org/10.1007/s00412-003-0237-5

Altendorfer, E., Lascarez-Lagunas, L. I., Nadarajan, S., Mathieson, I., & Colaiacovo, M. P. (2020). Crossover Position Drives Chromosome Remodeling for Accurate Meiotic

Chromosome Segregation. *Curr Biol*, *30*(7), 1329-1338 e1327. https://doi.org/10.1016/j.cub.2020.01.079

Barnes, T. M., Kohara, Y., Coulson, A., & Hekimi, S. (1995). Meiotic recombination, noncoding DNA and genomic organization in Caenorhabditis elegans. *Genetics*, *141*(1), 159-179. https://doi.org/10.1093/genetics/141.1.159

Bazan, G. C., & Hillers, K. J. (2011). SNP-based mapping of crossover recombination in Caenorhabditis elegans. *Methods Mol Biol*, *745*, 207-222. https://doi.org/10.1007/978-1-61779-129-1_13

Bean, C. J., Schaner, C. E., & Kelly, W. G. (2004). Meiotic pairing and imprinted X chromatin assembly in Caenorhabditis elegans. *Nat Genet*, *36*(1), 100-105. https://doi.org/10.1038/ng1283

Bergerat, A., de Massy, B., Gadelle, D., Varoutas, P. C., Nicolas, A., & Forterre, P. (1997). An atypical topoisomerase II from Archaea with implications for meiotic recombination. *Nature*, *386*(6623), 414-417. https://doi.org/10.1038/386414a0

Bernstein, M. R., & Rockman, M. V. (2016). Fine-Scale Crossover Rate Variation on the Caenorhabditis elegans X Chromosome. *G3 (Bethesda)*, *6*(6), 1767-1776. https://doi.org/10.1534/g3.116.028001

Bishop, H. I., Guan, D., Bocksteins, E., Parajuli, L. K., Murray, K. D., Cobb, M. M., Misonou, H., Zito, K., Foehring, R. C., & Trimmer, J. S. (2015). Distinct Cell- and Layer-Specific Expression Patterns and Independent Regulation of Kv2 Channel Subtypes in Cortical Pyramidal Neurons. *J Neurosci*, *35*(44), 14922-14942. https://doi.org/10.1523/JNEUROSCI.1897-15.2015

Botuyan, M. V., Lee, J., Ward, I. M., Kim, J. E., Thompson, J. R., Chen, J., & Mer, G. (2006). Structural basis for the methylation state-specific recognition of histone H4-K20 by 53BP1 and Crb2 in DNA repair. *Cell*, *127*(7), 1361-1373. https://doi.org/10.1016/j.cell.2006.10.043

Bouwman, P., Aly, A., Escandell, J. M., Pieterse, M., Bartkova, J., van der Gulden, H., Hiddingh, S., Thanasoula, M., Kulkarni, A., Yang, Q., Haffty, B. G., Tommiska, J., Blomqvist, C., Drapkin, R., Adams, D. J., Nevanlinna, H., Bartek, J., Tarsounas, M., Ganesan, S., & Jonkers, J. (2010). 53BP1 loss rescues BRCA1 deficiency and is associated with triple-negative and BRCA-mutated breast cancers. *Nat Struct Mol Biol*, *17*(6), 688-695. https://doi.org/10.1038/nsmb.1831

Brejc, K., Bian, Q., Uzawa, S., Wheeler, B. S., Anderson, E. C., King, D. S., Kranzusch, P. J., Preston, C. G., & Meyer, B. J. (2017). Dynamic Control of X Chromosome Conformation and Repression by a Histone H4K20 Demethylase. *Cell*, *171*(1), 85-102 e123. https://doi.org/10.1016/j.cell.2017.07.041

Bunting, S. F., Callen, E., Wong, N., Chen, H. T., Polato, F., Gunn, A., Bothmer, A., Feldhahn, N., Fernandez-Capetillo, O., Cao, L., Xu, X., Deng, C. X., Finkel, T., Nussenzweig, M., Stark, J. M., & Nussenzweig, A. (2010). 53BP1 inhibits homologous recombination in Brca1-deficient cells by blocking resection of DNA breaks. *Cell*, *141*(2), 243-254. https://doi.org/10.1016/j.cell.2010.03.012

Callen, E., Zong, D., Wu, W., Wong, N., Stanlie, A., Ishikawa, M., Pavani, R., Dumitrache, L. C., Byrum, A. K., Mendez-Dorantes, C., Martinez, P., Canela, A., Maman, Y., Day, A., Kruhlak, M. J., Blasco, M. A., Stark, J. M., Mosammaparast, N., McKinnon, P. J., & Nussenzweig, A. (2020). 53BP1 Enforces Distinct Pre- and Post-resection Blocks on

779 Homologous Recombination. *Mol Cell*, *77*(1), 26-38 e27.
780 https://doi.org/10.1016/j.molcel.2019.09.024
781 Cao, L., Xu, X., Bunting, S. F., Liu, J., Wang, R. H., Cao, L. L., Wu, J. J., Peng, T. N., Chen, J.,
782 Nussenzweig, A., Deng, C. X., & Finkel, T. (2009). A selective requirement for 53BP1 in
783 the biological response to genomic instability induced by Brca1 deficiency. *Mol Cell*,
784 *35*(4), 534-541. https://doi.org/10.1016/j.molcel.2009.06.037
785 Chapman, J. R., Barral, P., Vannier, J. B., Borel, V., Steger, M., Tomas-Loba, A., Sartori, A. A.,
786 Adams, I. R., Batista, F. D., & Boulton, S. J. (2013). RIF1 is essential for 53BP1-
787 dependent nonhomologous end joining and suppression of DNA double-strand break
788 resection. *Mol Cell*, *49*(5), 858-871. https://doi.org/10.1016/j.molcel.2013.01.002
789 Checchi, P. M., & Engebrecht, J. (2011). Caenorhabditis elegans histone methyltransferase
790 MET-2 shields the male X chromosome from checkpoint machinery and mediates
791 meiotic sex chromosome inactivation. *PLoS Genet*, *7*(9), e1002267.
792 https://doi.org/10.1371/journal.pgen.1002267
793 Chen, J., Li, P., Song, L., Bai, L., Huen, M. S. Y., Liu, Y., & Lu, L. Y. (2020). 53BP1 loss
794 rescues embryonic lethality but not genomic instability of BRCA1 total knockout mice.
795 *Cell Death Differ*, *27*(9), 2552-2567. https://doi.org/10.1038/s41418-020-0521-4
796 Chen, L., & Weir, J. R. (2024). The molecular machinery of meiotic recombination. *Biochem*
797 *Soc Trans*, *52*(1), 379-393. https://doi.org/10.1042/BST20230712
798 Colaiacovo, M. P., MacQueen, A. J., Martinez-Perez, E., McDonald, K., Adamo, A., La Volpe,
799 A., & Villeneuve, A. M. (2003). Synaptonemal complex assembly in C. elegans is
800 dispensable for loading strand-exchange proteins but critical for proper completion of
801 recombination. *Dev Cell*, *5*(3), 463-474. https://doi.org/10.1016/s1534-5807(03)00232-6
802 Cuella-Martin, R., Oliveira, C., Lockstone, H. E., Snellenberg, S., Grolmusova, N., & Chapman,
803 J. R. (2016). 53BP1 Integrates DNA Repair and p53-Dependent Cell Fate Decisions via
804 Distinct Mechanisms. *Mol Cell*, *64*(1), 51-64.
805 https://doi.org/10.1016/j.molcel.2016.08.002
806 Dernburg, A. F., McDonald, K., Moulder, G., Barstead, R., Dresser, M., & Villeneuve, A. M.
807 (1998). Meiotic recombination in C. elegans initiates by a conserved mechanism and is
808 dispensable for homologous chromosome synapsis. *Cell*, *94*(3), 387-398.
809 https://doi.org/10.1016/s0092-8674(00)81481-6
810 Difilippantonio, S., Gapud, E., Wong, N., Huang, C. Y., Mahowald, G., Chen, H. T., Kruhlak,
811 M. J., Callen, E., Livak, F., Nussenzweig, M. C., Sleckman, B. P., & Nussenzweig, A.
812 (2008). 53BP1 facilitates long-range DNA end-joining during V(D)J recombination.
813 *Nature*, *456*(7221), 529-533. https://doi.org/10.1038/nature07476
814 Dimitrova, N., Chen, Y. C., Spector, D. L., & de Lange, T. (2008). 53BP1 promotes non-
815 homologous end joining of telomeres by increasing chromatin mobility. *Nature*,
816 *456*(7221), 524-528. https://doi.org/10.1038/nature07433
817 El Mouridi, S., Alkhaldi, F., & Frokjaer-Jensen, C. (2022). Modular safe-harbor transgene
818 insertion for targeted single-copy and extrachromosomal array integration in
819 Caenorhabditis elegans. *G3 (Bethesda)*, *12*(9). https://doi.org/10.1093/g3journal/jkac184
820 Ellis, H. M., & Horvitz, H. R. (1986). Genetic control of programmed cell death in the nematode
821 C. elegans. *Cell*, *44*(6), 817-829. https://doi.org/10.1016/0092-8674(86)90004-8
822 Erdos, G., Pajkos, M., & Dosztanyi, Z. (2021). IUPred3: prediction of protein disorder enhanced
823 with unambiguous experimental annotation and visualization of evolutionary

conservation. *Nucleic Acids Res*, *49*(W1), W297-W303. https://doi.org/10.1093/nar/gkab408

Escribano-Diaz, C., & Durocher, D. (2013). DNA repair pathway choice--a PTIP of the hat to 53BP1. *EMBO Rep*, *14*(8), 665-666. https://doi.org/10.1038/embor.2013.99

Escribano-Diaz, C., Orthwein, A., Fradet-Turcotte, A., Xing, M., Young, J. T., Tkac, J., Cook, M. A., Rosebrock, A. P., Munro, M., Canny, M. D., Xu, D., & Durocher, D. (2013). A cell cycle-dependent regulatory circuit composed of 53BP1-RIF1 and BRCA1-CtIP controls DNA repair pathway choice. *Mol Cell*, *49*(5), 872-883. https://doi.org/10.1016/j.molcel.2013.01.001

Ferrari, M., Rawal, C. C., Lodovichi, S., Vietri, M. Y., & Pellicioli, A. (2020). Rad9/53BP1 promotes DNA repair via crossover recombination by limiting the Sgs1 and Mph1 helicases. *Nat Commun*, *11*(1), 3181. https://doi.org/10.1038/s41467-020-16997-w

Fradet-Turcotte, A., Canny, M. D., Escribano-Diaz, C., Orthwein, A., Leung, C. C., Huang, H., Landry, M. C., Kitevski-LeBlanc, J., Noordermeer, S. M., Sicheri, F., & Durocher, D. (2013). 53BP1 is a reader of the DNA-damage-induced H2A Lys 15 ubiquitin mark. *Nature*, *499*(7456), 50-54. https://doi.org/10.1038/nature12318

Gartner, A., & Engebrecht, J. (2022). DNA repair, recombination, and damage signaling. *Genetics*, *220*(2). https://doi.org/10.1093/genetics/iyab178

Gassmann, R., Rechtsteiner, A., Yuen, K. W., Muroyama, A., Egelhofer, T., Gaydos, L., Barron, F., Maddox, P., Essex, A., Monen, J., Ercan, S., Lieb, J. D., Oegema, K., Strome, S., & Desai, A. (2012). An inverse relationship to germline transcription defines centromeric chromatin in C. elegans. *Nature*, *484*(7395), 534-537. https://doi.org/10.1038/nature10973

Hariri, S., Li, Q., & Engebrecht, J. (2023). 53bp1 mutation enhances brca1 and bard1 embryonic lethality in C. elegans. *MicroPubl Biol*, *2023*. https://doi.org/10.17912/micropub.biology.000934

Hefel, A., Honda, M., Cronin, N., Harrell, K., Patel, P., Spies, M., & Smolikove, S. (2021). RPA complexes in Caenorhabditis elegans meiosis; unique roles in replication, meiotic recombination and apoptosis. *Nucleic Acids Res*, *49*(4), 2005-2026. https://doi.org/10.1093/nar/gkaa1293

Hodgkin, J. A., & Brenner, S. (1977). Mutations causing transformation of sexual phenotype in the nematode Caenorhabditis elegans. *Genetics*, *86*(2 Pt. 1), 275-287. https://www.ncbi.nlm.nih.gov/pubmed/560330

Irgen-Gioro, S., Yoshida, S., Walling, V., & Chong, S. (2022). Fixation can change the appearance of phase separation in living cells. *Elife*, *11*. https://doi.org/10.7554/eLife.79903

Iwabuchi, K., Bartel, P. L., Li, B., Marraccino, R., & Fields, S. (1994). Two cellular proteins that bind to wild-type but not mutant p53. *Proc Natl Acad Sci U S A*, *91*(13), 6098-6102. https://doi.org/10.1073/pnas.91.13.6098

Janisiw, E., Raices, M., Balmir, F., Paulin, L. F., Baudrimont, A., von Haeseler, A., Yanowitz, J. L., Jantsch, V., & Silva, N. (2020). Poly(ADP-ribose) glycohydrolase coordinates meiotic DNA double-strand break induction and repair independent of its catalytic activity. *Nat Commun*, *11*(1), 4869. https://doi.org/10.1038/s41467-020-18693-1

Jaramillo-Lambert, A., Ellefson, M., Villeneuve, A. M., & Engebrecht, J. (2007). Differential timing of S phases, X chromosome replication, and meiotic prophase in the C. elegans germ line. *Dev Biol*, *308*(1), 206-221. https://doi.org/10.1016/j.ydbio.2007.05.019

Jaramillo-Lambert, A., & Engebrecht, J. (2010). A single unpaired and transcriptionally silenced X chromosome locally precludes checkpoint signaling in the Caenorhabditis elegans germ line. *Genetics*, *184*(3), 613-628. https://doi.org/10.1534/genetics.109.110338

Jaramillo-Lambert, A., Harigaya, Y., Vitt, J., Villeneuve, A., & Engebrecht, J. (2010). Meiotic errors activate checkpoints that improve gamete quality without triggering apoptosis in male germ cells. *Curr Biol*, *20*(23), 2078-2089. https://doi.org/10.1016/j.cub.2010.10.008

Jullien, D., Vagnarelli, P., Earnshaw, W. C., & Adachi, Y. (2002). Kinetochore localisation of the DNA damage response component 53BP1 during mitosis. *J Cell Sci*, *115*(Pt 1), 71-79. https://doi.org/10.1242/jcs.115.1.71

Jumper, J., Evans, R., Pritzel, A., Green, T., Figurnov, M., Ronneberger, O., Tunyasuvunakool, K., Bates, R., Zidek, A., Potapenko, A., Bridgland, A., Meyer, C., Kohl, S. A. A., Ballard, A. J., Cowie, A., Romera-Paredes, B., Nikolov, S., Jain, R., Adler, J., . . . Hassabis, D. (2021). Highly accurate protein structure prediction with AlphaFold. *Nature*, *596*(7873), 583-589. https://doi.org/10.1038/s41586-021-03819-2

Kaur, T., & Rockman, M. V. (2014). Crossover heterogeneity in the absence of hotspots in Caenorhabditis elegans. *Genetics*, *196*(1), 137-148. https://doi.org/10.1534/genetics.113.158857

Keeney, S., Giroux, C. N., & Kleckner, N. (1997). Meiosis-specific DNA double-strand breaks are catalyzed by Spo11, a member of a widely conserved protein family. *Cell*, *88*(3), 375-384. https://doi.org/10.1016/s0092-8674(00)81876-0

Kelly, W. G., Schaner, C. E., Dernburg, A. F., Lee, M. H., Kim, S. K., Villeneuve, A. M., & Reinke, V. (2002). X-chromosome silencing in the germline of C. elegans. *Development*, *129*(2), 479-492. https://doi.org/10.1242/dev.129.2.479

Kilic, S., Lezaja, A., Gatti, M., Bianco, E., Michelena, J., Imhof, R., & Altmeyer, M. (2019). Phase separation of 53BP1 determines liquid-like behavior of DNA repair compartments. *EMBO J*, *38*(16), e101379. https://doi.org/10.15252/embj.2018101379

Kramer, M., Kranz, A. L., Su, A., Winterkorn, L. H., Albritton, S. E., & Ercan, S. (2015). Developmental Dynamics of X-Chromosome Dosage Compensation by the DCC and H4K20me1 in C. elegans. *PLoS Genet*, *11*(12), e1005698. https://doi.org/10.1371/journal.pgen.1005698

Lascarez-Lagunas, L. I., Martinez-Garcia, M., Nadarajan, S., Diaz-Pacheco, B. N., Berson, E., & Colaiacovo, M. P. (2023). Chromatin landscape, DSB levels, and cKU-70/80 contribute to patterning of meiotic DSB processing along chromosomes in C. elegans. *PLoS Genet*, *19*(1), e1010627. https://doi.org/10.1371/journal.pgen.1010627

Lawrence, K. S., Chau, T., & Engebrecht, J. (2015). DNA damage response and spindle assembly checkpoint function throughout the cell cycle to ensure genomic integrity. *PLoS Genet*, *11*(4), e1005150. https://doi.org/10.1371/journal.pgen.1005150

Li, M., Cole, F., Patel, D. S., Misenko, S. M., Her, J., Malhowski, A., Alhamza, A., Zheng, H., Baer, R., Ludwig, T., Jasin, M., Nussenzweig, A., Serrano, L., & Bunting, S. F. (2016). 53BP1 ablation rescues genomic instability in mice expressing 'RING-less' BRCA1. *EMBO Rep*, *17*(11), 1532-1541. https://doi.org/10.15252/embr.201642497

Li, Q., Hariri, S., & Engebrecht, J. (2020). Meiotic Double-Strand Break Processing and Crossover Patterning Are Regulated in a Sex-Specific Manner by BRCA1-BARD1 in Caenorhabditis elegans. *Genetics*, *216*(2), 359-379. https://doi.org/10.1534/genetics.120.303292

Li, Q., Kaur, A., Okada, K., McKenney, R. J., & Engebrecht, J. (2023). Differential requirement for BRCA1-BARD1 E3 ubiquitin ligase activity in DNA damage repair and meiosis in the Caenorhabditis elegans germ line. *PLoS Genet*, *19*(1), e1010457. https://doi.org/10.1371/journal.pgen.1010457

Lim, J. G., Stine, R. R., & Yanowitz, J. L. (2008). Domain-specific regulation of recombination in Caenorhabditis elegans in response to temperature, age and sex. *Genetics*, *180*(2), 715-726. https://doi.org/10.1534/genetics.108.090142

Link, J., Paouneskou, D., Velkova, M., Daryabeigi, A., Laos, T., Labella, S., Barroso, C., Pacheco Pinol, S., Montoya, A., Kramer, H., Woglar, A., Baudrimont, A., Markert, S. M., Stigloher, C., Martinez-Perez, E., Dammermann, A., Alsheimer, M., Zetka, M., & Jantsch, V. (2018). Transient and Partial Nuclear Lamina Disruption Promotes Chromosome Movement in Early Meiotic Prophase. *Dev Cell*, *45*(2), 212-225 e217. https://doi.org/10.1016/j.devcel.2018.03.018

MacQueen, A. J., Colaiacovo, M. P., McDonald, K., & Villeneuve, A. M. (2002). Synapsis-dependent and -independent mechanisms stabilize homolog pairing during meiotic prophase in C. elegans. *Genes Dev*, *16*(18), 2428-2442. https://doi.org/10.1101/gad.1011602

Mets, D. G., & Meyer, B. J. (2009). Condensins regulate meiotic DNA break distribution, thus crossover frequency, by controlling chromosome structure. *Cell*, *139*(1), 73-86. https://doi.org/10.1016/j.cell.2009.07.035

Mirman, Z., & de Lange, T. (2020). 53BP1: a DSB escort. *Genes Dev*, *34*(1-2), 7-23. https://doi.org/10.1101/gad.333237.119

Mirman, Z., Lottersberger, F., Takai, H., Kibe, T., Gong, Y., Takai, K., Bianchi, A., Zimmermann, M., Durocher, D., & de Lange, T. (2018). 53BP1-RIF1-shieldin counteracts DSB resection through CST- and Polalpha-dependent fill-in. *Nature*, *560*(7716), 112-116. https://doi.org/10.1038/s41586-018-0324-7

Mirza-Aghazadeh-Attari, M., Mohammadzadeh, A., Yousefi, B., Mihanfar, A., Karimian, A., & Majidinia, M. (2019). 53BP1: A key player of DNA damage response with critical functions in cancer. *DNA Repair (Amst)*, *73*, 110-119. https://doi.org/10.1016/j.dnarep.2018.11.008

Monen, J., Maddox, P. S., Hyndman, F., Oegema, K., & Desai, A. (2005). Differential role of CENP-A in the segregation of holocentric C. elegans chromosomes during meiosis and mitosis. *Nat Cell Biol*, *7*(12), 1248-1255. https://doi.org/10.1038/ncb1331

Nabeshima, K., Villeneuve, A. M., & Hillers, K. J. (2004). Chromosome-wide regulation of meiotic crossover formation in Caenorhabditis elegans requires properly assembled chromosome axes. *Genetics*, *168*(3), 1275-1292. https://doi.org/10.1534/genetics.104.030700

Noordermeer, S. M., Adam, S., Setiaputra, D., Barazas, M., Pettitt, S. J., Ling, A. K., Olivieri, M., Alvarez-Quilon, A., Moatti, N., Zimmermann, M., Annunziato, S., Krastev, D. B., Song, F., Brandsma, I., Frankum, J., Brough, R., Sherker, A., Landry, S., Szilard, R. K., . . . Durocher, D. (2018). The shieldin complex mediates 53BP1-dependent DNA repair. *Nature*, *560*(7716), 117-121. https://doi.org/10.1038/s41586-018-0340-7

O'Connell, K. F., Caron, C., Kopish, K. R., Hurd, D. D., Kemphues, K. J., Li, Y., & White, J. G. (2001). The C. elegans zyg-1 gene encodes a regulator of centrosome duplication with distinct maternal and paternal roles in the embryo. *Cell*, *105*(4), 547-558. https://doi.org/10.1016/s0092-8674(01)00338-5

961 Paiano, J., Wu, W., Yamada, S., Sciascia, N., Callen, E., Paola Cotrim, A., Deshpande, R. A.,
962 Maman, Y., Day, A., Paull, T. T., & Nussenzweig, A. (2020). ATM and PRDM9 regulate
963 SPO11-bound recombination intermediates during meiosis. *Nat Commun*, *11*(1), 857.
964 https://doi.org/10.1038/s41467-020-14654-w
965 Paix, A., Folkmann, A., Rasoloson, D., & Seydoux, G. (2015). High efficiency, homology-
966 directed genome editing in *Caenorhabditis elegans* ssing CRISPR-Cas9
967 ribonucleoprotein complexes. *Genetics*, *201*(1), 47-54.
968 https://doi.org/10.1534/genetics.115.179382
969 Phillips, C. M., & Dernburg, A. F. (2006). A family of zinc-finger proteins is required for
970 chromosome-specific pairing and synapsis during meiosis in C. elegans. *Dev Cell*, *11*(6),
971 817-829. https://doi.org/10.1016/j.devcel.2006.09.020
972 Phillips, C. M., Wong, C., Bhalla, N., Carlton, P. M., Weiser, P., Meneely, P. M., & Dernburg,
973 A. F. (2005). HIM-8 binds to the X chromosome pairing center and mediates
974 chromosome-specific meiotic synapsis. *Cell*, *123*(6), 1051-1063.
975 https://doi.org/10.1016/j.cell.2005.09.035
976 Prigent, C., & Dimitrov, S. (2003). Phosphorylation of serine 10 in histone H3, what for? *J Cell*
977 *Sci*, *116*(Pt 18), 3677-3685. https://doi.org/10.1242/jcs.00735
978 Reuben, M., & Lin, R. (2002). Germline X chromosomes exhibit contrasting patterns of histone
979 H3 methylation in Caenorhabditis elegans. *Dev Biol*, *245*(1), 71-82.
980 https://doi.org/10.1006/dbio.2002.0634
981 Rinaldo, C., Bazzicalupo, P., Ederle, S., Hilliard, M., & La Volpe, A. (2002). Roles for
982 Caenorhabditis elegans rad-51 in meiosis and in resistance to ionizing radiation during
983 development. *Genetics*, *160*(2), 471-479. https://doi.org/10.1093/genetics/160.2.471
984 Rocha, P. P., Raviram, R., Fu, Y., Kim, J., Luo, V. M., Aljoufi, A., Swanzey, E., Pasquarella, A.,
985 Balestrini, A., Miraldi, E. R., Bonneau, R., Petrini, J., Schotta, G., & Skok, J. A. (2016).
986 A Damage-Independent Role for 53BP1 that Impacts Break Order and Igh Architecture
987 during Class Switch Recombination. *Cell Rep*, *16*(1), 48-55.
988 https://doi.org/10.1016/j.celrep.2016.05.073
989 Rockman, M. V., & Kruglyak, L. (2009). Recombinational landscape and population genomics
990 of Caenorhabditis elegans. *PLoS Genet*, *5*(3), e1000419.
991 https://doi.org/10.1371/journal.pgen.1000419
992 Ryu, J. S., Kang, S. J., & Koo, H. S. (2013). The 53BP1 homolog in C. elegans influences DNA
993 repair and promotes apoptosis in response to ionizing radiation. *PLoS One*, *8*(5), e64028.
994 https://doi.org/10.1371/journal.pone.0064028
995 Saito, T. T., Lui, D. Y., Kim, H. M., Meyer, K., & Colaiacovo, M. P. (2013). Interplay between
996 structure-specific endonucleases for crossover control during Caenorhabditis elegans
997 meiosis. *PLoS Genet*, *9*(7), e1003586. https://doi.org/10.1371/journal.pgen.1003586
998 Schmiedeberg, L., Skene, P., Deaton, A., & Bird, A. (2009). A temporal threshold for
999 formaldehyde crosslinking and fixation. *PLoS One*, *4*(2), e4636.
1000 https://doi.org/10.1371/journal.pone.0004636
1001 Schultz, L. B., Chehab, N. H., Malikzay, A., & Halazonetis, T. D. (2000). p53 binding protein 1
1002 (53BP1) is an early participant in the cellular response to DNA double-strand breaks. *J*
1003 *Cell Biol*, *151*(7), 1381-1390. https://doi.org/10.1083/jcb.151.7.1381
1004 Solinger, J. A., Kiianitsa, K., & Heyer, W. D. (2002). Rad54, a Swi2/Snf2-like recombinational
1005 repair protein, disassembles Rad51:dsDNA filaments. *Mol Cell*, *10*(5), 1175-1188.
1006 https://doi.org/10.1016/s1097-2765(02)00743-8

1007 Sundaravinayagam, D., Rahjouei, A., Andreani, M., Tupina, D., Balasubramanian, S., Saha, T.,
1008 Delgado-Benito, V., Coralluzzo, V., Daumke, O., & Di Virgilio, M. (2019). 53BP1
1009 Supports Immunoglobulin Class Switch Recombination Independently of Its DNA
1010 Double-Strand Break End Protection Function. *Cell Rep*, *28*(6), 1389-1399 e1386.
1011 https://doi.org/10.1016/j.celrep.2019.06.035
1012 Teves, S. S., An, L., Hansen, A. S., Xie, L., Darzacq, X., & Tjian, R. (2016). A dynamic mode of
1013 mitotic bookmarking by transcription factors. *Elife*, *5*.
1014 https://doi.org/10.7554/eLife.22280
1015 Tock, A. J., & Henderson, I. R. (2018). Hotspots for Initiation of Meiotic Recombination. *Front*
1016 *Genet*, *9*, 521. https://doi.org/10.3389/fgene.2018.00521
1017 Usui, T., & Shinohara, A. (2021). Rad9, a 53BP1 Ortholog of Budding Yeast, Is Insensitive to
1018 Spo11-Induced Double-Strand Breaks During Meiosis. *Front Cell Dev Biol*, *9*, 635383.
1019 https://doi.org/10.3389/fcell.2021.635383
1020 Vielle, A., Lang, J., Dong, Y., Ercan, S., Kotwaliwale, C., Rechtsteiner, A., Appert, A., Chen, Q.
1021 B., Dose, A., Egelhofer, T., Kimura, H., Stempor, P., Dernburg, A., Lieb, J. D., Strome,
1022 S., & Ahringer, J. (2012). H4K20me1 contributes to downregulation of X-linked genes
1023 for C. elegans dosage compensation. *PLoS Genet*, *8*(9), e1002933.
1024 https://doi.org/10.1371/journal.pgen.1002933
1025 Wang, H., Peng, B., Pandita, R. K., Engler, D. A., Matsunami, R. K., Xu, X., Hegde, P. M.,
1026 Butler, B. E., Pandita, T. K., Mitra, S., Xu, B., & Hegde, M. L. (2017). Aurora kinase B
1027 dependent phosphorylation of 53BP1 is required for resolving merotelic kinetochore-
1028 microtubule attachment errors during mitosis. *Oncotarget*, *8*(30), 48671-48687.
1029 https://doi.org/10.18632/oncotarget.16225
1030 Ward, I. M., Minn, K., Jorda, K. G., & Chen, J. (2003). Accumulation of checkpoint protein
1031 53BP1 at DNA breaks involves its binding to phosphorylated histone H2AX. *J Biol*
1032 *Chem*, *278*(22), 19579-19582. https://doi.org/10.1074/jbc.C300117200
1033 Ward, I. M., Minn, K., van Deursen, J., & Chen, J. (2003). p53 Binding protein 53BP1 is
1034 required for DNA damage responses and tumor suppression in mice. *Mol Cell Biol*,
1035 *23*(7), 2556-2563. https://doi.org/10.1128/MCB.23.7.2556-2563.2003
1036 Ward, I. M., Reina-San-Martin, B., Olaru, A., Minn, K., Tamada, K., Lau, J. S., Cascalho, M.,
1037 Chen, L., Nussenzweig, A., Livak, F., Nussenzweig, M. C., & Chen, J. (2004). 53BP1 is
1038 required for class switch recombination. *J Cell Biol*, *165*(4), 459-464.
1039 https://doi.org/10.1083/jcb.200403021
1040 Weinert, T., & Hartwell, L. (1989). Control of G2 delay by the rad9 gene of Saccharomyces
1041 cerevisiae. *J Cell Sci Suppl*, *12*, 145-148.
1042 https://doi.org/10.1242/jcs.1989.supplement_12.12
1043 Wells, M. B., Snyder, M. J., Custer, L. M., & Csankovszki, G. (2012). Caenorhabditis elegans
1044 dosage compensation regulates histone H4 chromatin state on X chromosomes. *Mol Cell*
1045 *Biol*, *32*(9), 1710-1719. https://doi.org/10.1128/MCB.06546-11
1046 Wilson, M. D., Benlekbir, S., Fradet-Turcotte, A., Sherker, A., Julien, J. P., McEwan, A.,
1047 Noordermeer, S. M., Sicheri, F., Rubinstein, J. L., & Durocher, D. (2016). The structural
1048 basis of modified nucleosome recognition by 53BP1. *Nature*, *536*(7614), 100-103.
1049 https://doi.org/10.1038/nature18951
1050 Woglar, A., & Villeneuve, A. M. (2018). Dynamic Architecture of DNA Repair Complexes and
1051 the Synaptonemal Complex at Sites of Meiotic Recombination. *Cell*, *173*(7), 1678-1691
1052 e1616. https://doi.org/10.1016/j.cell.2018.03.066

Wood, W. B., Hecht, R., Carr, S., Vanderslice, R., Wolf, N., & Hirsh, D. (1980). Parental effects and phenotypic characterization of mutations that affect early development in Caenorhabditis elegans. *Dev Biol*, *74*(2), 446-469. https://doi.org/10.1016/0012-1606(80)90445-5

Yim, H., Shin, S. B., Woo, S. U., Lee, P. C., & Erikson, R. L. (2017). Plk1-mediated stabilization of 53BP1 through USP7 regulates centrosome positioning to maintain bipolarity. *Oncogene*, *36*(7), 966-978. https://doi.org/10.1038/onc.2016.263

Yokoo, R., Zawadzki, K. A., Nabeshima, K., Drake, M., Arur, S., & Villeneuve, A. M. (2012). COSA-1 reveals robust homeostasis and separable licensing and reinforcement steps governing meiotic crossovers. *Cell*, *149*(1), 75-87. https://doi.org/10.1016/j.cell.2012.01.052

Yuan, J., Shaham, S., Ledoux, S., Ellis, H. M., & Horvitz, H. R. (1993). The C. elegans cell death gene ced-3 encodes a protein similar to mammalian interleukin-1 beta-converting enzyme. *Cell*, *75*(4), 641-652. https://doi.org/10.1016/0092-8674(93)90485-9

Zhang, L., Geng, X., Wang, F., Tang, J., Ichida, Y., Sharma, A., Jin, S., Chen, M., Tang, M., Pozo, F. M., Wang, W., Wang, J., Wozniak, M., Guo, X., Miyagi, M., Jin, F., Xu, Y., Yao, X., & Zhang, Y. (2022). 53BP1 regulates heterochromatin through liquid phase separation. *Nat Commun*, *13*(1), 360. https://doi.org/10.1038/s41467-022-28019-y

Figure S1. Localization and phenotype of HSR-9 fusions and mutants. A) Cartoon of *hsr-9* gene structure indicating position of fusions, and mutant alleles. B) % embryonic lethality of wild type (WT) (26), *hsr-9(xoe17)* (23), *brc-1(xoe4)* (12), *hsr-9(xoe17); brc-1(xoe4)* (25), *gfp::V5::hsr-9* (11), *hsr-9::gfp::3xHA* (10), *gfp::V5::hsr-9; brc-1(xoe4)* (12); *hsr-9::gfp::3xHA; brc-1(xoe4)* (11). Number of animals examined are in paratheses. Mean and 95% Confidence Interval shown; *** $p < 0.001$; ** $p < 0.01$; * $p < 0.05$ by Mann-Whitney. C) Images of HSR-9::GFP fluorescence from indicated regions of the germ line. PZ = proliferative zone; TZ = transition zone; EP = early pachytene; MP = mid pachytene; LP = late pachytene; DP = diplotene; DK = diakinesis. Scale bar = 10µm.

Figure S2. Meiotic Recombination in *hsr-9* mutants. A) Percent embryonic lethality in the apoptosis-defective *ced-3(ok2734)* mutant and *hsr-9(xoe17); ced-3(ok2734)* double mutant, n = 10 worms for each genotype. B) Coefficient of Variation (CV) of GFP::RPA-1 fluorescence was measured from 6 germlines in the pachytene region of the germ line in *gfp::rpa-1* and *hsr-9(ok759); gfp::rpa-1* worms using the 3i spinning disc microscope. C) Box whisker plots show number of RAD-51 foci per nucleus in the indicated regions. Horizontal line of each box represents the median, top and bottom of each box represents medians of upper and lower quartiles, lines extending above and below boxes indicate SD, and individual data points are outliers from 5 to 95%. Statistical significant comparisons by Mann–Whitney of WT vs. *hsr-9(ok759)* and *hsr-9(xoe17)* are indicated; ***$p< 0.0001$. D) Dissected germ lines immunolabelled with

RAD-51 (red) and counterstained with DAPI (blue) in WT, *hsr-9(xoe17), rad-54(ok615)* and *hsr-9(xoe17); rad-54(ok615)* worms.

Figure 1

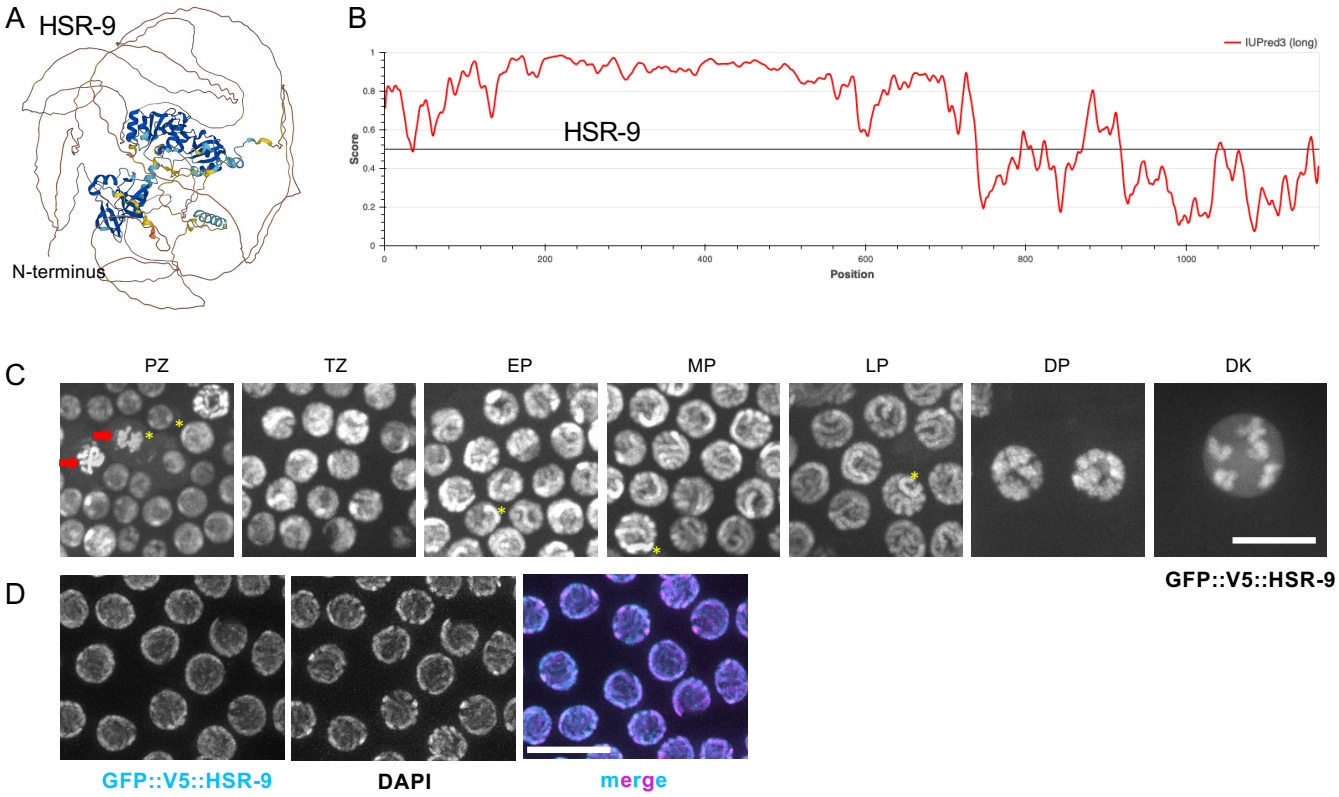

Figure 2

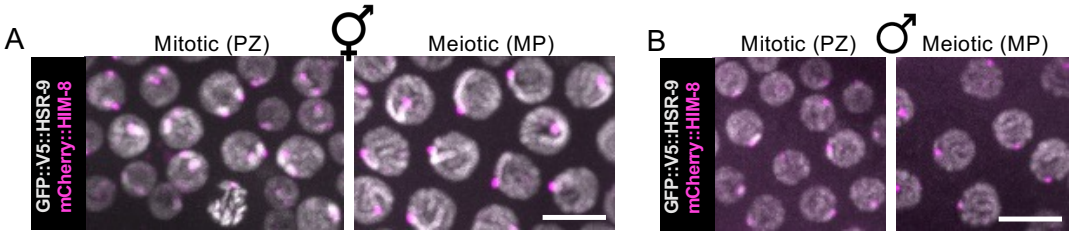

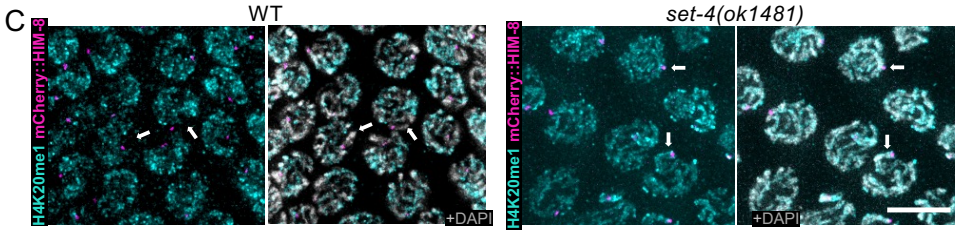

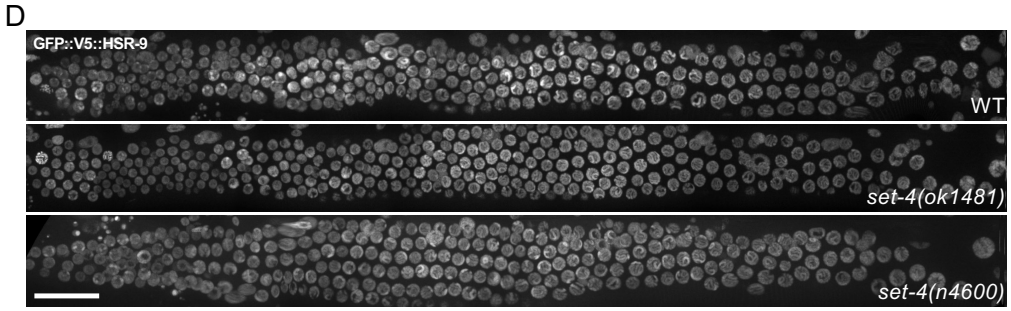

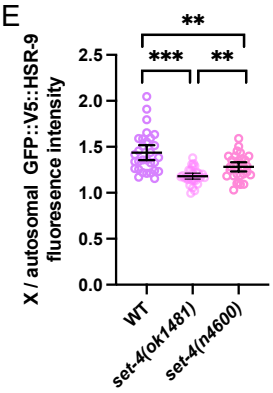

Figure 3

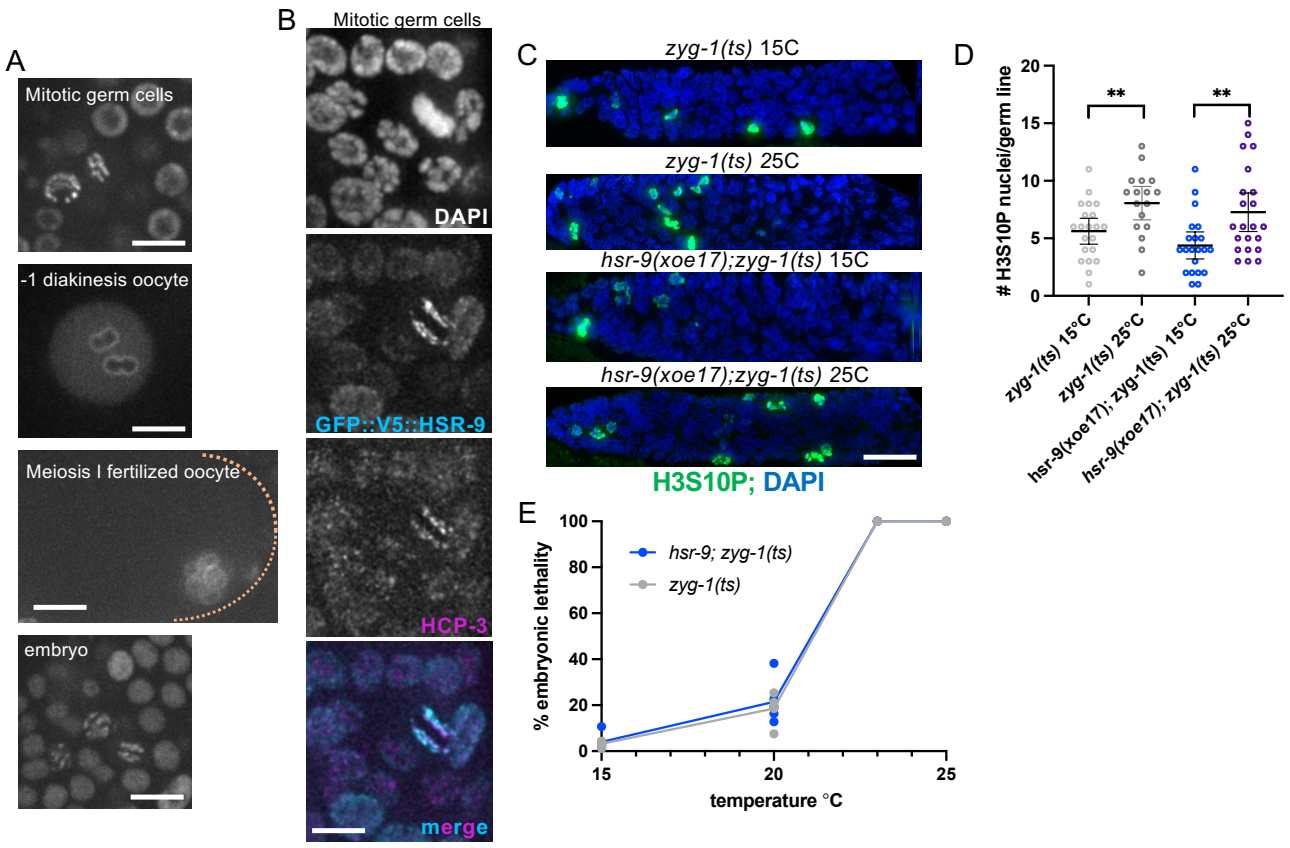

Figure 4

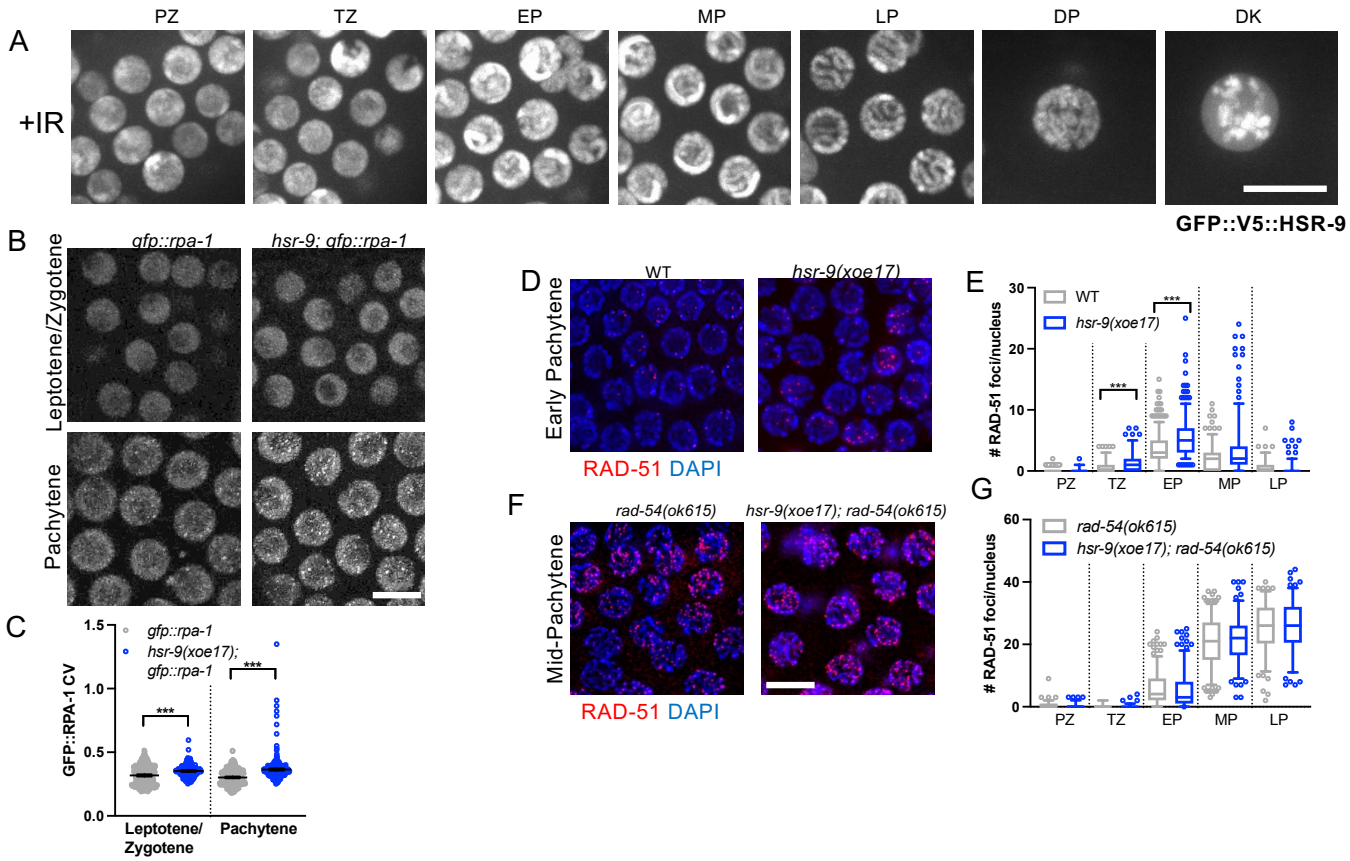

Figure 5

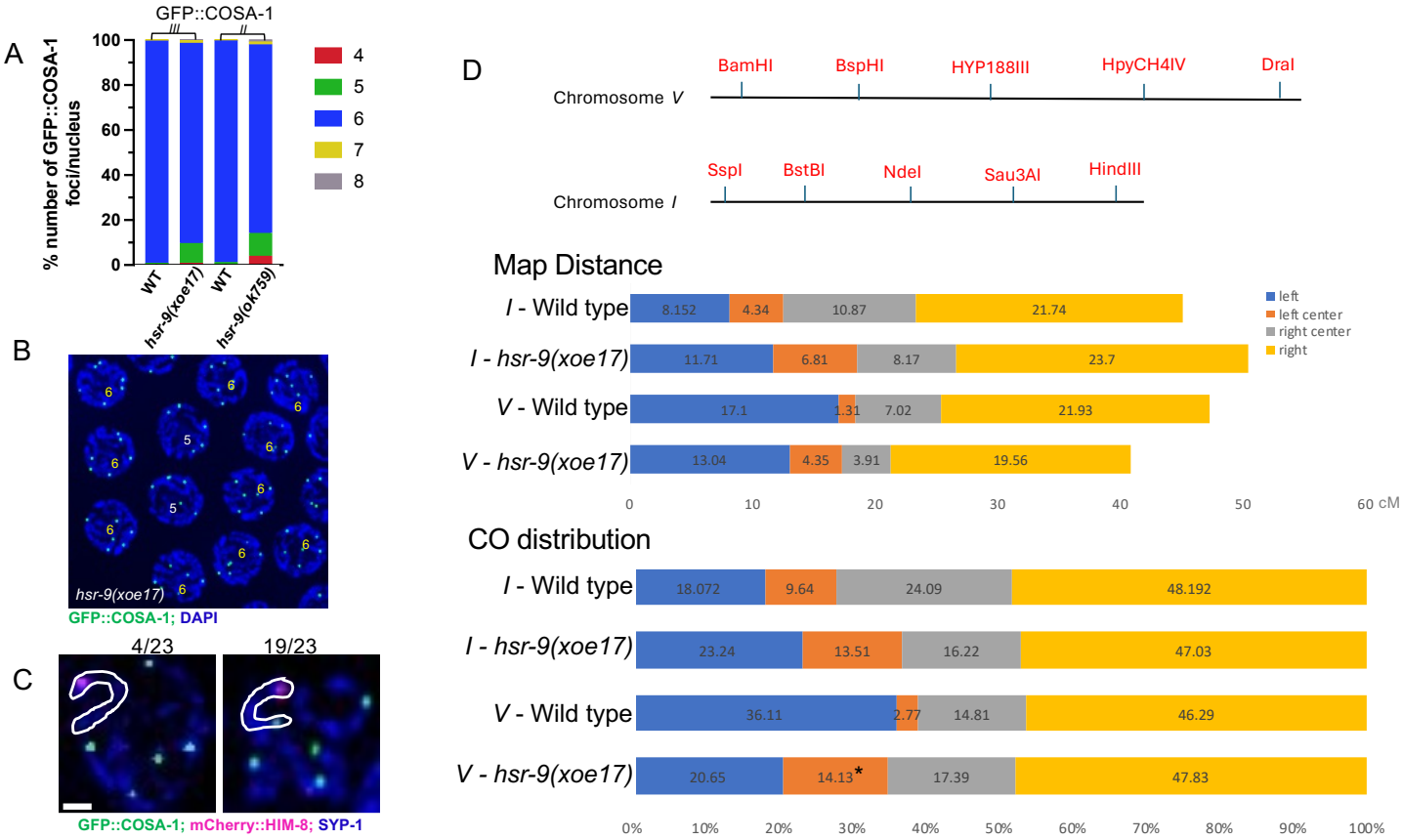

Figure 6

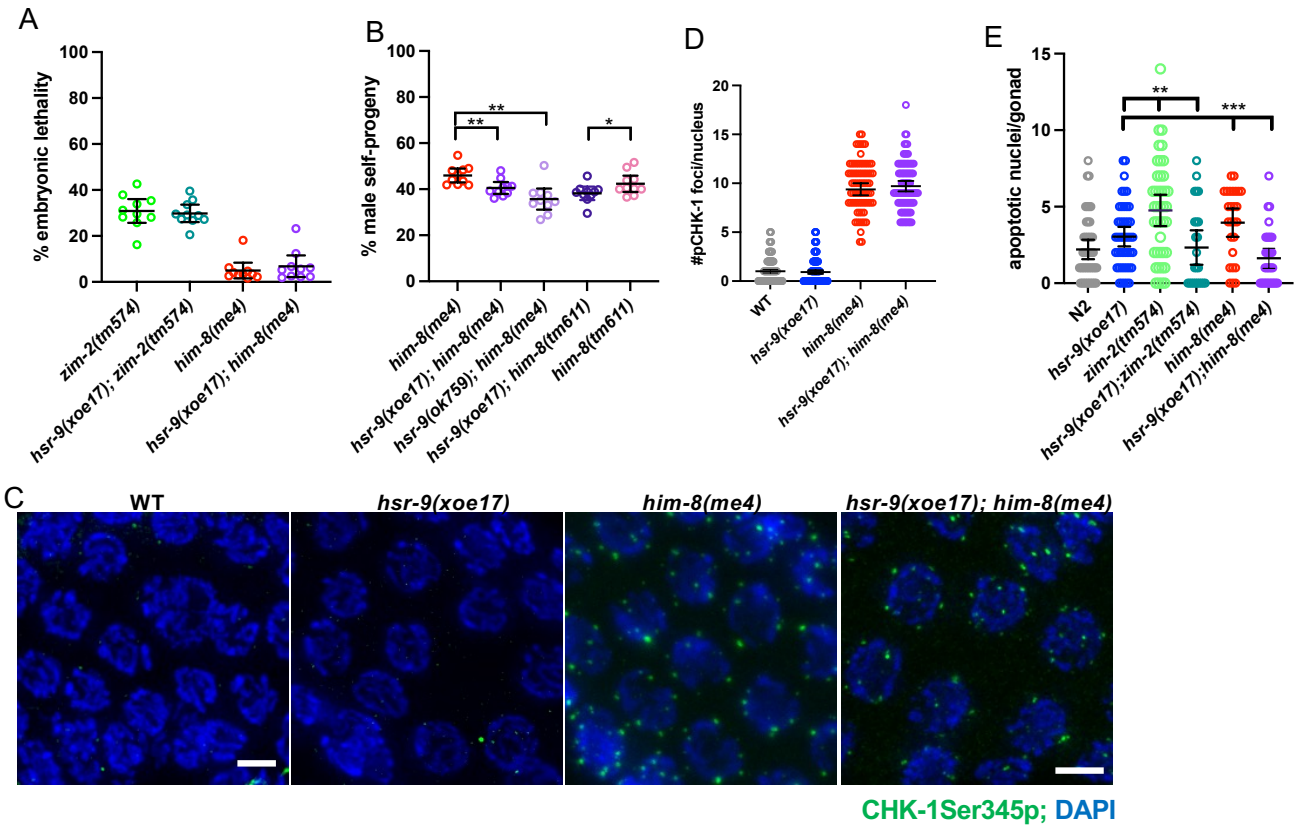

Figure 7

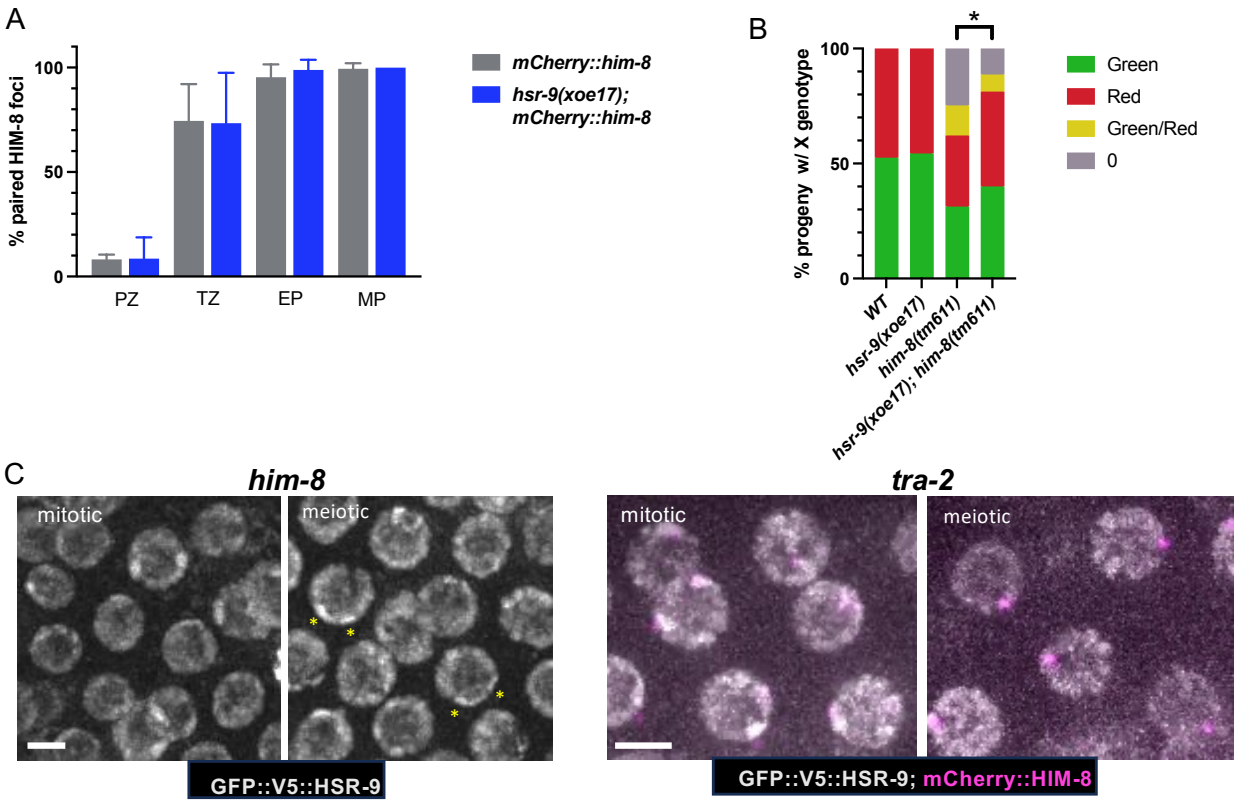

Figure S1

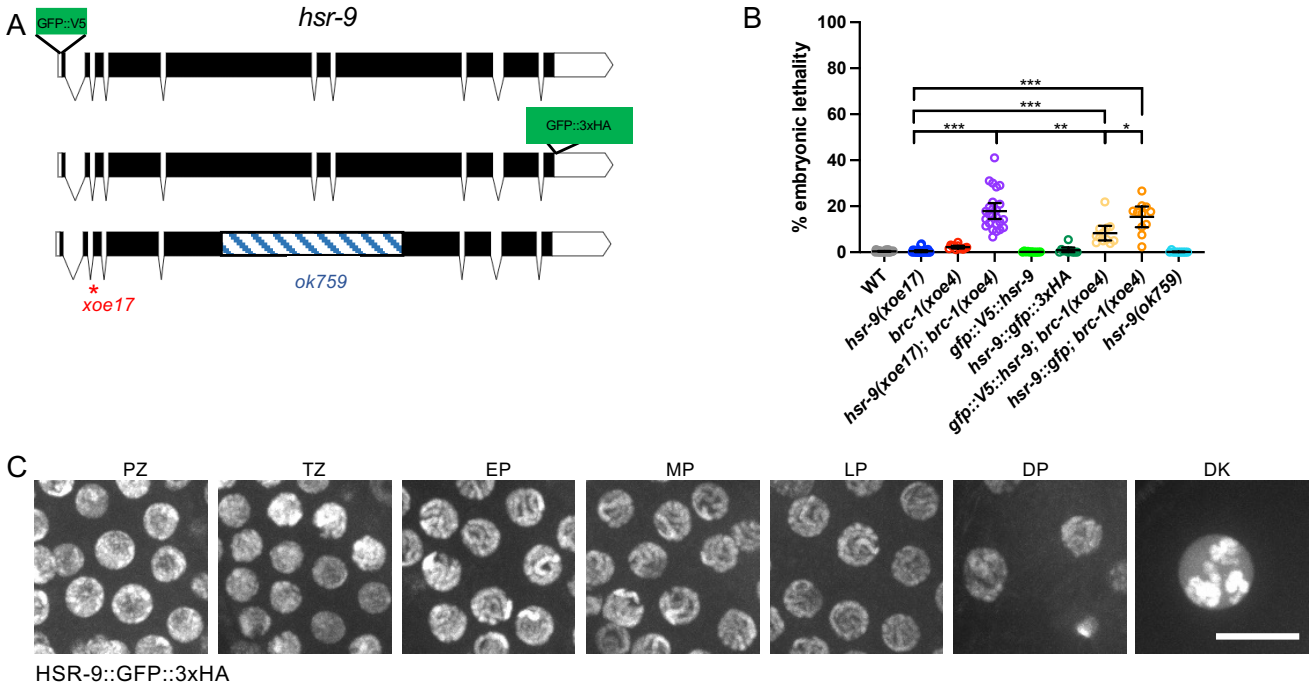

Figure S2